Dear Editor,

Thank you for providing the opportunity to respond to all reviewer's comments with a revised version of our paper:

Title: Analysis Algorithm for Sky Type and Ice Halo Recognition in All-Sky Images
Author(s): Sylke Boyd et al.
MS No.: amt-2018-401
MS Type: Research article
Iteration: Revised Submission

We are thankful to you and the reviewers for providing feedback and necessary comments. We believe the revisions helped to improve the manuscript significantly with respect to clarity, organization, and relation to the existing body of work in the field. While we already responded to individual reviewer comments in the discussion of the paper, please find below a complete list of all responses and revisions.

Unfortunately, when implementing the reviewer's suggestions, we revised the paper not in a mode that tracked changes, but rather highlighted the implemented changes. Hopefully, this will not impede your decision process. Revisions in response to reviewer 1 were highlighted in yellow, revisions for reviewer 2 in gray. Additional revisions after reviewer responses are included in the tracking of changes. If you prefer we rework the responses to reviewers in a mode that tracks changes instead, please advise us to do so. We will go back to make such adjustments.

One major change is the addition of a figure as a new Fig.1. Reviewer 2 laid open problems in the flow of the article that appeared to be mostly related to unclear presentation on how the different parts of the algorithm work together. Hopefully, the inclusion of a flow chart in the new Fig. 1 will address this problem effectively.

We look forward to hear from you about a decision on whether these revisions are acceptable for publication.

Sincerely,

Sylke Boyd (corresponding author)

Re: amt-2018-401-RC1

Author's Response to Comments by Reviewer 1

The authors would like to thank reviewer 1 for the thorough and helpful comments to our manuscript "Analysis Algorithm for Sky Type and Ice Halo Recognition in All-Sky Images". We have incorporated many of the suggestions. The paper has improved significantly thanks to the thorough attention to detail given by reviewer 1. We are much obliged, and extend our gratitude.

Below, we outline the details on changes made to the manuscript in response to the comments.

> General: The introduction is missing one important motivation for detecting halos. One main reason why detection of halos is relevant is that the pristine crystals that produce them have scattering phase functions with less pronounced backscattering than those of the amorphous or roughened crystals that do not produce halos (Yang et al 2015). As crystal roughness or distortion increase, their phase functions are characterized by decreasing halo features (van Diedenhoven 2014) and decreasing asymmetry parameters
> (van Diedenhoven et al. 2014; Yang et al 2015). Ice particle surface roughening has a significant influence on the global cloud radiative effect (Yi et al. 2013). Some text along these lines, with the relevant references needs to be included in the introduction.

This is a very good point to make, thank you! Text was inserted in the Introduction to address this concern (page 2, lines 26 to 35)

"As shown in theoretical studies (van Diedenhoven, 2014; Yang et al., 2015), halos form in particular if the ice crystals exhibit smooth surfaces. In that case, the forward scattered intensity is much more pronounced as in cases of rough surfaces, even if a crystal habit is present. If many of the ice particles are amorphous in nature, or did not form under conditions of crystal growth- for example by freezing from super-cooled droplets, or by riming – the forward scattering pattern will be weaker, and similar to what we see for liquid droplets: a white scattering disk surrounding the sun, but no halo. In turn, roughness and asymmetry of ice crystals influence the magnitude of backscattered solar radiation, thus influencing the radiative effect of cirrus clouds (van Diedenhoven, 2016). If the particles in the cirroform cloud are very small, e.g. a few microns (Sassen, 1991), diffraction will lead to a corona. Hence, we believe that a systematic observation of the optical scattering properties adds information to our data on cirrus composition and cirrus radiative properties."

> Page 2, lines 7 and 11: Replace Knobelspiesse et al., 2015 with Waliser et al. (2009).

Reference to Waliser et al. (2009) was added in line 7. The reference to Knobelspiesse et al, 2015. had already been changed after the editor's request. In line 11, we replaced the reference to Knobelspiesse et al., 2015 with the suggested reference.

> Page 2, line 12: Here it is stated that "Cloud particle sizes can range from 0.1 microns to a few millimetres (Cziczo and Froyd, 2014)." I think few microns to a few millimetres (or even centimeters) is more realistic. Also, I suggest to replace the reference with Heymsfield et al. (2013).

Correction to "few microns to even centimeter sizes" was incorporated, and a reference to Heymsfield et al (2013) was added. The Cziczo and Froyd article is a review paper, reviewing particle size distributions from various measurements.

Page 2, line 12: Replace the reference to Delene, 2011 with Heymsfield et al. (2013)

Correction was incorporated.

Line 15: add Hong et al. (2016) to the reference on lidar/radar.

Reference was reviewed and added.

Line 20: I suggest to replace all references here with Bailey and Hallet (2009); Baran (2009) and Yang et al (2015).

The references in line 21 have been corrected as suggested.

Line 21: It is not very clear what is meant with "observable symmetric scattering patterns", but it seems that "halo displays" may be more appropriate. Also note in the sentence that smooth crystal surfaces are needed for halos. Please add references to Um and McFarquhar (2015) and van Diedenhoven (2014)

The sentence has been rephrased to "Only ice particles with a simple crystal habit and smooth surfaces can lead to halo displays", and the suggested references have been added.

Line 24: In reference to the "additional ice halo features" cite the book of Tape and Moilanen (2006).

The citation was inserted.

Line 26: Add "forward" before "scattering"

The word was added to the sentence.

On line 27, discussing the corona, refer to Sassen (1991). Also a more realistic size for corona producing ice crystals is "a few microns".

The wording was changed according to the suggestion. The proposed reference was inserted.

Line 31: The presentation at the Gordon Research Conference on Radiation and Climate in 2015 cannot be considered a published result, so please remove the reference.
In any case, I thought this sentence was very confusing as I thought this was referencing to the results presented in this paper. I suggest to remove this part.

The sentence and reference was removed.

Line 32: The reference to Seefeldner is incorrect and should be Forster et al. 2017.

The previous change removed this reference.

Section 1
Page 4: line 14: I suggest to replace "start the master table" with "train the algorithm", as the master table is not introduced yet.

(now line 10) The correction was inserted.

Section 2.1

Page 5, line 12: A value for pre-factor C_0 is given, but the X is not defined yet. I suggest to give a value for C_0 later.

We replaced the sentence with "The pre-factor C_0 in Eqn.(6) is chosen later to place the values for F into a convenient number range." Renumbering the equations resulted in the shift in Eqn number.

Page 5: equation 3: Do the absolute values of the elements in x need to be similar so they are weighted equally? Please explain in the text.

We inserted the following sentence in the hope this would clarify the issue: "For the image properties we chose in STS and IHS computation, the elements of X_{image} lie within one order of magnitude of each other. Hence, no weighing became necessary for this application." Renumbering the equations moved former Eqn (3) to Eqn (6).

Section 2.2
Page 5;, line 26: What are the units for BGR? Is that one byte?

The color values in the jpg have no defined unit, but scale with the receive intensity of the light. We hope to have clarified this by inserting the following statement: "Every pixel in a TSI image exhibits a value between 0 and 255 for each of the three colour channels blue (B), green (G), and red (R). The colour values represent the intensity of the colour channel registered for the particular pixel, varying between 0 (no intensity) and 255 (brightest possible)."

Page 6: line 13: Add "to" between "and" and "then".

Correction was applied.

Page 6 (and elsewhere): Use equation numbers for each equation and expressions throughout the paper.

We renumbered the equations, and included all of them.

Page 6: line 5, what is "B" here? In the previous it references to Blue, but the expression is used for all colors. Please clarify in the text.

Equation (8) was modified to include the tinting procedure as done for every color channel in each pixel.

Page 6: line 7: Remove the brackets and make the text explaining alpha into a proper sentence.

We included this correction: "The coefficient ⍺ regulates the strength of the tinting such that ⍺=0 leads to no tint, and ⍺=1 produces an image of a single colour." (now page 6, line 13/14)

Figure 2: Define RAI, TL, TR, BL, BR in caption.

The caption was modified to include "The LSM is divided into four quadrants, named according to their position as TR – top right, BR – bottom right, BL – bottom left, and TL – top left. The RAI is the Radial Analysis Interval for which STS and IHS properties are evaluated."

Section 2.3
Page 7: line 6: What are the units of I(s)?

We added the following sentence to the text: "The term intensity refers to the colour values of any of the colour channels, and varies between 0 and 255."

Page 7: line 12: Replace "A cloudy sky" with "An overcast sky".

Now page 7, line 20: the correction has been made.

> Page 7: line 19: Use italics for "s"

This has been corrected after the editorial request, perhaps. I am not sure what it refers to?

> Figure 3 (and 6): Please add proper x-axis labels. There is an "s" in the corner. Please spell out "radial distance" and place in the center. I also suggest to add the labels to the bottom of the bottom figures and add a dotted line indicating the zero deviation.

The suggested changes to the figures have been implemented.

> Page 8: line 11: replace CLR with "clear".

Correction was included, now on line 21.

> Page 8: line 16: It is noted that the "mechanism described in section 2.1" is used. Be explicit about the properties discussed here are inserted in X? Also, I suggest to provide the value of C_0 here.

We hope that the following modification explains the process better (now page 8 lines 27 to 33):

"We are using the mechanism described in section **Error! Reference source not found.**, Eqns (1) through (6). The continually refined master table defines a mean value vector M, see Eqn (2), and inverse covariance matrix Σ^{-1}, see Eqn (4), for each sky type. The mean values for M are given in **Error! Reference source not found.**, together with their standard deviations for the training set of images. As a new image is processed, its STS property vector X, Eqn (1), is computed for each sky quadrant. Subsequently, a score is computed for each sky type using Eqn. (6). A value of 10^5 was used for C_0 which places a rough separator of order 1 between images that match closely a particular sky type, and those which do not."

> Figure 4: Please add y-axis labels. AST in the caption should be ASD.

Corrections were made as suggested.

> Figure 5: Black arrows are used to match the images to the timeline, but these arrows are not visible on the black indicating CS. I propose pointing the arrows of the top images to the top of the timeline plot, so that they are visible.

The adjustments to the figure have been made as suggested, and an error in the caption was corrected.

> Page 9: line 30: It is mentioned that "if a radial sequence is found in one colour channel, it should be found in the same locations in all colour channels". Should the angular difference between colors of the halo not be taken into account? The red part of the halo is closer to the sun.

There are multiple factors that influence the inability of the algorithm to resolve the color channels. The first is the small size of the TSI images. Even under good lighting conditions, the angular resolution is limited to 0.3°, particularly near the horizon. When the perspective distortion is removed, a further reduction in resolution is introduced, again particularly affecting near-horizon solar positions at zenith angles above 45°. That affects the majority of images. The third influence lies in uncertainties in the solar position. Even though a series of calibrations can address any minor misalignments in North-south line, zenith position, mirror-camera alignment, shadow strip position etc, they are manually assigned, and introduce another uncertainty that affects the fine-angle resolution.

The wording was changed to "Lastly, a radial sequence should be consistent across all three colour channels,…" to avoid potential confusion.

Section 3
Page 11, line 23: Some caution is rightfully raised about the visual classification. Somemore information on the method would be helpful to include in the text (here or above at the start of section 3). For example, who was doing the classifications? Is that one person, all of the authors, other people? Also, my guess is that the person (or persons?) evaluating the images are not doing this blindly, so they might already be biased towards the classification of the algorithm.

The training of the algorithm is a give-and-take, with the goal to maximize agreement. Visual inspection is not perfect, and neither is the algorithm. We modified page 11, lines 8 through 19 to try to address some of the reviewer's concerns: "For each of the 31 days of March, an observer assigned sky classifications to segments of the day by inspecting the day series as an animation. This can easily be done by using an image viewer and continuously scrolling through the series. Then, the day would be subjected to the algorithm. The sections of the record in which visual and algorithm differed were inspected again, at which point either the visual assessment was adjusted, or the misclassified images were included in the Master table in order to train the algorithm toward better recognition. Adjustment to visual classifications often occurred at the fringes of a transition. For example, when a sky transitions from cirrostratus to altostratus to stratus, the transitions are not sharp. The observer sets an image as the point in which the sky moved from CS to CLD, but the criteria in the algorithm would still indicate CS. This can affect up to a hundred images at transition times, which then were reclassified. On the other hand, if a clearly visible halo was missed by the algorithm, this would be a case for adding new property lines to the Master table in order to capture the particular conditions. After each change in the Master table, the algorithm would be repeated, and recalibrations to the visual record, as well as to the Master table itself were made. The process was repeated several times until no more gains in accuracy were observed. These adjustments were done by SB."

Page 13, line 3-4: For clarity add "in Table 6" after the "second set of numbers". I suggest to remove the part ", which may be a little easier to interpret".

The text has been adjusted accordingly, now page 13, line 29.

Page 13: It might be good to discuss the results somewhat more in comparison to Forster et al. 2017.

Absolutely. Since submitting this paper, long-year analyses of the TSI record have been undertaken, which show some really interesting seasonal variations in the halo appearances in CS skies. We find maximum halo fraction in CS of 20-25% of all CS skies in March and April, consistently through several years of records. We presented that on a poster at the AMS which can be found online if there is interest. This will give a much better basis for comparison than the four-month record included in this paper. We included some more language on page 13 lines 22 to 25 and 30 to address this concern.

"in particular with respect to assessments of variation of smooth versus rough crystals. Forster et al (Forster et al., 2017) discuss that the necessary fraction of smooth crystals for a halo appearance lies between 10% and 40%. The authors observe a 22° halo for 25% of all cirrus clouds for a 2.5-year

photographic record taken in Munich, Germany." And "This is certainly consistent with the observations of Forster et al (Forster et al., 2017)."

Re: amt-2018-401-RC1

Author's Response to Comments by Reviewer 2

I would like to thank reviewer 2 for the time taken to read, understand, and thoughtfully comment on our manuscript. The reviewers comments have been very detailed and targeted, and have helped to improve the manuscript significantly. It is the hope of the authors that this means the reviewer does not consider the work presented here as hopeless, but was mostly concerned with the clarity of presentation.

Below, I will address the concerns expressed in the reviewer's comments and indicate where and which actions were taken to improve the manuscript in response. The response follows the outline of RC2 closely, and is organized as required by the editor

    (1) comments from Referees,

    (2) author's response,

    (3) author's changes in manuscript for each applicable comment.

The adjustments in response to reviewer 1 are highlighted in yellow, while the adjustments included for reviewer 2 are highlighted in gray in the attached manuscript.

Thank you again for your time and valuable input.

Sylke Boyd

Begin response:

Major remarks:

(1) As visible in Fig. 5, identifying a 22º halo in TSI images might be challenging (even visually) due to a relatively coarse resolution, stray light, and over-exposed image regions. On the upside, TSI cameras are widely used, hence providing a large dataset from several geographic locations which is very attractive for long-term intercomparison studies.

(2) I do agree that there are limitations to the resolution of TSI images. These limitations are discussed in the manuscript line 10, page 4 (revised according to recommendations from reviewer 2). It is not difficult to visually identify halos in a TSI series if one considers subsequent images in context. For example, cloud features will move, while 22° halos stay stationary with respect to the sun. That is why the algorithm includes the Gaussian time broadening in equation 14. Clearly, clarification is in order. Section 1 has been expanded accordingly, see in the detailed responses below.

(1) The method used to calculate the 22⁰ halo score has considerable overlap with Forster et al. 2017: features are determined in order to discriminate images containing a 22⁰ halo from images which don't. It would be valuable to discuss the slightly differing choice of these features compared to Forster et al. Please discuss the impact of image resolution/FOV of TSI images on the choice of features. The presented study determines the threshold for labelling the images as "22⁰ halo" and "no 22⁰ halo" manually in contrast to Forster et al., who utilized a machine learning method. Please discuss the merits of the different approach used here.

(2) There are multiple differences and similarities.

In common:

- Using the radial intensity, and searching for a series of properties of that radial intensity in order to identify halos. Both methods find use in the sequence of a minimum, followed by a maximum in radial intensity.
- The use of a training set, and evaluation in a set of images not used for training.
- The success rates in identifying 22° halos are similar. Forster algorithm predicts 97.3 +/- 1.9% accuracy of halo in the top segment, 88.5+/- 7.1% accuracy of halo in the bottom segment of the solar surroundings. While we have not inspected the accuracy by sky quadrant, and while our algorithm does not produce a binary decision, the IHS can be used to produce a binary decision if so desired. In section 3, we introduced a decision threshold for the IHS, and we have found that 88% of our algorithm's halo identifications indeed correspond to a visual halo. That is a success rate comparable to Forster. Both algorithms are secure in decisions of "no halo"

Differences:

- Objective: Forster et al constructed a high-resolution camera with precision control for positioning, allowing a much more precise and highly resolved imaging of the sky surrounding the sun. In consequence, the algorithm developed by Forster et al is able to resolve color dispersion in halo display, in addition to specifically search for halo features such as parhelia, upper tangential arcs, etc. Therefore, the outcomes are different. The TSI images targeted in this manuscript do not allow the search for parhelia, nor for color dispersion, due to limitations in resolution. Our objective is to extract not only halo information, but also sky type information.
- Resolution: employing a precision camera allows complete control over angular variables gleaned from the images. This precision in measuring angles is then used in the algorithm of Forster in searching for halo minimum and maximum in precise locations. That is not the case for the TSI algorithm in this manuscript. The limitations of resolution, and the variety of imperfections in alignments and perspective resolution made it necessary to work out a method that is self-consistent in its units, but not necessarily mapping to objective angles.
- Halo characterization process: Forster et al uses a decision tree constructed from random forest classifiers. It is a classification scheme that is correctly characterized as a machine learning algorithm. The criteria governing the final decision tree are derived from a training set of images. The Forster algorithm arrives at a binary classification halo/no halo. Instead of a decision tree, we employed multivariate analysis and

investigated Mahalanobis distances to regions of interest in the space of properties. Defining these regions (means and covariance matrix) is a continued process, which certainly can be called training. The result, however, is not a binary decision, rather a halo score along a continuous scale, which rates how much an image resembles the reference halo images. It is incorrect to characterize this as "labelling the images as "22⬜ halo" and "no 22⬜ halo" manually ".

The continuous halo score is assigned to an image by the algorithm. If, upon further data analysis, one attempts to use it for a yes/no decision then the application of a threshold becomes necessary. But that is not part of the algorithm itself. In section 3, the manuscript discusses applications of the algorithm, together with a thorough test of its capabilities. That is where a decision threshold is introduced.

- The TSI algorithm introduced here analyses sky type in addition to searching for ice halo features.

I would like to add, that the concern for the considerable overlap is justified. It is interesting, that Forster and the authors of this manuscript arrived at the very same points to characterize halos independently. We (SB and MK) met Linda Forster at the 2015 Gordon Conference on Radiation and Climate, introducing these exact two algorithms. The difference in publication date lies in the difference between what can be done in a pure research environment, and what can be done in an institution where research involves only undergraduate students, including the continued and repeated training and time constraints present here. However, that should not have any bearing on the manuscript. I added a paragraph to section 3.

(3)page 16, line1 ff Finally, it is worth discussing the general approach of the TSI algorithm in comparison to the halo detection algorithm developed by Forster et al (Forster et al., 2017). Both algorithms utilize features found in the radial intensity $I(s)$, such as the sequence of minimum – maximum at the expected radial positions in order to find halos in an image. The random forest classifier approach described in (Forster et al., 2017) is a machine learning approach that arrives at a binary conclusion for an image in form of halo/no halo. Their algorithm was trained on a visually classified set of images in order to construct a suitable decision tree. In addition to 22°halos, the Forster algorithm also identifies parhelia and other ice halo features in images taken by a high-resolution, sun-tracking halo camera. The algorithm presented here for TSI data must work with a much less specialized set of images, notably of lower resolution. It does not characterize halos in a binary decision, but rather assigns a continuous ice halo score to an image, in addition to sky type scores for four different types of sky conditions. Similar to the Forster algorithm, the TSI algorithm also was trained on a visually classified set of images. Further training is easy to incorporate via a master table which provides means and covariance matrices to the algorithm. Both algorithm have overlap. The TSI algorithm makes extensive use of the radial brightness gradient (slope) for the sky type assignments. The relation of this gradient to the physical presence of scatterers along the optical path makes this an attractive approach.

(1) How exactly was the algorithm trained? In order to assess its ability to correctly assign the labels "22º halo" and "no 22º halo" as well as the 4 different sky types, it is common practice to test the trained algorithm against *independent* images, which were excluded from the training data. Please describe how exactly this algorithm was tested.

(2) Exactly. That is why we used 80 seed images to define criteria, and to "seed" the master table. This is mentioned in section 1, page 4 line 14, in the sentence "We used eighty seed images taken from across the TSI record and across all available years to train the algorithm (ENA, 2018; NSA, 2018; SGP, 2018). This included images visually identified as CS, PCL, CLD, CLR, and halo-bearing. The seed samples were used to develop the algorithm and define a suitable set of characteristic properties for STS and IHS. " The description of the training method is contained in section 3, page 11, line 8ff. This section was expanded significantly in response to reviewer 1. Here is the new section to address this concern:

(3) Page 11, line13 ff: For each of the 31 days of March, an observer assigned sky classifications to segments of the day by inspecting the day series as an animation. This can easily be done by using an image viewer and continuously scrolling through the series. Then, the day would be subjected to the algorithm. The sections of the record in which visual and algorithm differed were inspected again, at which point either the visual assessment was adjusted, or the misclassified images were included in the Master table in order to train the algorithm toward better recognition. Adjustment to visual classifications often occurred at the fringes of a transition. For example, when a sky transitions from cirrostratus to altostratus to stratus, the transitions are not sharp. The observer sets an image as the point in which the sky moved from CS to CLD, but the criteria in the algorithm would still indicate CS. This can affect up to a hundred images at transition times, which then were reclassified. On the other hand, if a clearly visible halo was missed by the algorithm, this would be a case for adding new property lines to the Master table in order to capture the particular conditions. After each change in the Master table, the algorithm would be repeated, and recalibrations to the visual record, as well as to the Master table itself were made. The process was repeated several times until no more gains in accuracy were observed. These adjustments were done by SB.

---

(1) Over-exposed image regions are mentioned several times (e.g. P11, L17). Please discuss their impact on the image classification. How was over-exposure treated in general? How would you assess the influence of over-exposed pixels to the detection of 22º halos?

(2) Table 2 contains a fifth sky classification: N/A. Overexposure is easily identified: if the average radial color values in the analysis region are above a threshold (used 253) in each color channel then the computation of any further properties is compromised. This particular sky quadrant is excluded from skytype assignments as well as halo analysis. It may be worth to remember that the analysis area lies between 15 and 25 LSM units in the local sky map, which excludes the sun itself. As a practical matter, overexposure is a signal produced often in images taken at solar positions near the horizon (discussed in section 2.3.2, page 9, line 31). It is influenced by the

perspective correction, which lowers resolution significantly under these conditions. Perhaps, the inclusion of the following statement can help clarify this in the manuscript.

(3) Pg 9, line 13ff: It simply means that its properties are not close to any of the sky type categories. Also classified as N/A are quadrants in which the average radial intensity lies above 253 (overexposure), or contains a large fraction of horizon (bottom quadrants in low sun positions).

---

(1) How was ensured that parhelia were not accidentally misclassified as 22º halos at low elevations of the sun?

(2) Low sun positions, which are more prone to lead to parhelia appearances, are victim to low resolution due to perspective distortion. The resolution vertically falls below 1.2°. I have not been able to visually and reliably discriminate parhelia in any TSI image. An algorithm specifically for parhelia was therefore not attempted. With the separation into quadrants, any existing parhelia would form right on the boundary between top and bottom quadrant , and basically average into the radial intensity of this quadrant. The algorithm does mark N/A for the bottom quadrants at low solar positions, since the local sky map contains mostly horizon for those quadrants. The top quadrants, if not overexposed, may give halo signals. But again – parhelia can not be visually distinguished in those images.

---

(1) The definition and choice of the four sky types should be explained in the text. Halo displays can form in cirrocumulus and optically thick cirrus clouds as well. It is mentioned several times throughout the manuscript that the sky type classification of the images is used to infer information about the "presence of smooth crystalline habits among the cloud particles" (e.g. P13, L6). To answer that question it would be necessary to differentiate between ice clouds and other sky types including clear sky, as in Sassen et al. 2003 and Forster et al. 2017. Thus, the choice of sky types in this study, seems to be not ideal and aims more at differentiating cloud cover ("clear" vs. "cloudy" vs. "partially cloudy", cf. P11, L4). The definition of "cirrostratus" seems to be limited to optically thin, homogeneous cirrus. However, ice clouds and thus halo displays could also be connected with a "cloudy" as well as "partially cloudy" sky type (cf. P9, L10/11) or even "clear" for very thin cirrus (cf. P11, L26-29). Please re-assess the choice of sky type classes regarding the interpretation of the results.

(2) The reviewer's comments in this point seem to be concerned with a bias in the halo search, introduced by an assumption of cirrostratus necessary to detect a halo? Proceeding with this assumption.

Please understand that STS and IHS are assigned independently from each other, and use differing sets of criteria. Even if some of the criteria are similar, the master training yields different averages and covariances. The slopes for CS and for IHS are numerically different (and all other common properties are as well) as can be seen from comparison of tables 3 (STS properties) and 4 (IHS properties). As a matter of fact, we do find ice halos in both PCL and CLD

skies, as explained in section 3, page 14, lines 25ff. Section 2.3.2 describes the selection of sky types to be scored. Since we focus on the areas of the sky in which a 22° halo would be located, the sky type really only characterizes the radial analysis area indicated in Figure 2, not the complete visual sky. The beginning of section 2.3.1 explicitly explains why the radial intensity is the key for the chosen sky types, in that the average gradient contains a measure of number and density of scatterers in that sky area.

I would like to add, that the reviewer statement
> "It is mentioned several times throughout the manuscript that the sky type classification of the images is used to infer information about the "presence of smooth crystalline habits among the cloud particles" (e.g. P13, L6)."

indicates a misunderstanding. The whole sentence (now pg15 line 25) reads
> "One of the conclusion to be made from the relation between STS and IHS concerns the confidence in the presence of smooth crystalline habits among the cloud particles, as shown only in a one-fifth fraction of all cirrostratus."

It is not the STS alone that can give information about the type of ice crystals, but the combination of STS and IHS. That is an important distinction. It means that if cirrostratus is present, we can conclude with confidence that halo-generating habits are present if a halo is detected, and that occurs for about 20% of all cirrostratus occurrences in the data set analyzed in this manuscript. This is addressed in the detailed responses below.

---

(1) Finally, "long-term data / image records" is mentioned several times (e.g. P1, L6; P3, L19; P13, L13) and Table 1 refers to multiple datasets spanning up to about 7 years of data. I see this as a potential major advantage of this study. However, the study evaluates only images of one ARM site (Southern Great Plains) from January through April 2018. Please describe only the data that was actually used (cf. Tab. 1 and the statement on P2, L30/31). If the algorithm is applicable to large long-time datasets, why wasn't this exploited?

(2) The reviewer is correct. The longest data set is actually 18 years long. The manuscript under review here is a method paper, in which an algorithm is introduced in detail, together with reasonably long test data to demonstrate effectiveness and limitations. This is laid out in the Introduction, now page 3, line23ff.

The explicit analysis of the long-term records in different geographical locations will require a separate paper, to be expanded and supported by LIDAR data. The summary has language to that strategy. In addition, this work is done at an undergraduate institution, with undergraduate research assistants, including all the time and training restrictions this brings. Data collection and analysis will take time. Some of the additional findings have already been published at the 99th AMS meeting (https://ams.confex.com/ams/2019Annual/meetingapp.cgi/Paper/351343), and more is going to be ready by the end of summer 2019.

The long-term data records are included in this current manuscript since the set of 80 seed images is taken evenly from all three locations and different times. Section 2 already discusses this. I changed the table caption to include this fact as well, hoping to improve clarity.

(3) **Table 1. TSI data set properties. Seed images for the algorithm were taken from all three locations.**

(1) The introduction could be tailored more towards implications of unknown cirrus optical and microphysical properties, especially ice crystal shape (and orientation), on the Earth's radiation budget and satellite remote sensing of cirrus clouds. The selection of literature should be revised in this context, with an emphasis on primary literature, especially on the formation and frequency of halo displays (e.g. Minnaert (1937), Tricker (1970), Greenler (1980), Tape (1994), Tape and Moilanen (2006)), as well as ice crystal microphysical properties (e.g. Magono and Lee (1966), Bailey and Hallett (2009)). For example, as a reference for the various ice crystal sizes (P2, L13) and shapes (P2 L20), literature on in situ observations would be more suitable. Delene 2011 and Ewald et al. 2013, for example, don't seem to be the primary literature to support the statement.

(2) Reviewer 1 had similar comments about the introduction. In response, the set of references as well as the wording has been revised considerably. I hope this also addresses some of the concerns expressed by reviewer 2.That

Specific comments on the manuscript:
Introduction

(1) P2, L16-17: "All of these methods are restricted to a particular time…It is clear that no single method has all the composition information", please clarify. This statement seems to be inherent of any kind of measurement. What exactly should be pointed out here? How do TSI observations solve this problem?

(2) Great point about the measurements. What should be said here is that despite the existence of so many approaches to cirrus measurements, the composition information has gaps. TSI analysis for ice halos may provide another support that can fill some of these gaps. I replaced the sentence with this:

(3) Pg 2 ln 16ff: Even combined, these methods leave gaps in our knowledge of spatial and temporal composition of ice clouds. The analysis of ice halos as captured by long-term total sky imagers may provide further insight and allow to close some of the gaps.

(1) P2, L24: "More symmetry in the particle orientations will add additional ice halofeatures." Which additional features? Please cite corresponding literature.

(2) Information and reference was added.

(3) Pg 2, ln 25: More symmetry in the particle orientations will add additional ice halo features such as parhelia, upper tangent arc, circumscribed halo, and others (Greenler, 1980; Tape and Moilanen, 2006)

---

(1) P3, L11: "The fraction of smooth crystals necessary for ice halo appearance is 10% for columns, and 40% for plates (van Diedenhoven, 2014)". It should be added that these results represent a lower threshold and are based on analysis of scattering phase functions. Therefore, they are not directly applicable to observations of 22 · halos in the atmosphere including multiple scattering.

(2) Language to this extend has been included. I would like to add that the prevalence of multiple scattering will generally lead to a dissolution of the halo display. We see that in thickening altostratus clouds, when a halo perhaps still shows in some images, but it is "washed" out by increasing attenuation. So, at the very least one can conclude two things from a halo display: (a) a minimum of 10-40% smooth enough crystalline ice particles, and (b) dominance of single scattering. Unfortunately, I do not think that the latter has been quantified yet.

(3) Pg 3, 14ff: The fraction of smooth crystals necessary for ice halo appearance is at a minimum10% for columns, and 40% for plates, based on an analysis of scattering phase functions for single scattering events (van Diedenhoven, 2014). While this establishes a lower boundary, it is correct to say that the observability of an ice halo allows to conclude that smooth crystalline ice particles are present and single-scattering events dominate. The consideration of the percentage of cirrus clouds that display optical halo features allows therefore, upon further study, inferences about the microphysical conditions in the cloud.

---

(1) P3, L12-14: "The consideration of the percentage of cirrus clouds that display optical halo features allows a direct conclusion with respect to the fraction of crystalline habit in the cloud, and, upon further study, about the microphysical conditions in the cloud." The fraction of hexagonal crystals in cirrus clouds cannot be directly inferred from the frequency of visible halo displays. Beside the single scattering properties, which van Diedenhoven 2014 investigated, multiple scattering has to be considered (cf. Forster et al. 2017).

(2) Addressed in previous.

---

(1) P3, L28: "refinement of the algorithm goals" is unclear in this context, please elaborate.

(2) Changed wording.
(3) Pg 3, ln 32: Section **Error! Reference source not found.** presents the details of the image analysis algorithm, including subsections on algorithm goals, image preparation, and sky type and halo scoring.

---

1 TSI images □

(1) P4, L11: Please provide a range for the angular resolution, specifically for the camera (SGP) and time period used in this study.

(2) An image from SGP in 2018 has a size of 488 by 640 pixels. The short dimension limits the radius of the view circle, let's say it is 240 pixels. A pixel close to the center corresponds to an angular sky section 2.8⁰ wide and 0.24⁰ tall. In the TSI series analyzed here, the solar position never reaches this point. Close to the horizon, one pixels averages a sky section that is 0.24⁰ wide and 1.24⁰ tall. Best resolution is achieved at zenith angle 45⁰, in which case every pixel represents a sky region of 0.33⁰ by 0.33⁰. Language indicating this has been included in section 1.

(3) Pg 4, ln 14ff: ~~The angular resolution varies with zenith angle but can rise above 0.7 ° for the smaller images (0.4° for the larger size), in particular for sky sections close to the horizon.~~ For example, an image from SGP taken in 2018 has a size of 488 by 640 pixels. The short dimension limits the radius of the view circle to at most 240 pixels. A pixel close to the center of the view circle corresponds to an angular sky section 2.8⁰ wide and 0.24⁰ tall. At SGP, the solar position never reaches this point. Close to the horizon, one pixels averages a sky section that is 0.24⁰ wide and 1.24⁰ tall. Best resolution is achieved at zenith angle 45⁰, in which case every pixel represents a sky region of 0.33⁰ by 0.33⁰. The image distortion is largest for sky segments close to the horizon due to perspective distortions in the mirror image of the sky.

2 Algorithm

2.1 Goal and Strategy

(1) P5, L7: What is C0 ? Normalization constant? Explanation in L12 should be moved here.
(2) Reviewer 1 had a similar comment. In response, the following wording has been applied:
(3) Pg 5 ln 27: … improvement of scoring. The pre-factor C_0 in Equation (6) is chosen later to place the values for F into a convenient number range. This basic alg..

2.2 Image preparations and local sky map (LSM)

(2) This particular section seems to be written in a confusing manner, as I conclude from the many questions targeting similar issues. I have re-organized it to first list the calibration steps in order and then describe the details of each of the steps.

(3) pg 6 ln2 ff: The image preparations include the following steps: (1) a colour correction, (2) an alignment calibration, (3) a removal of the perspective distortion, (4) masking and marking of the solar position, and (5) rotation and crop to create a Local Sky Map (LSM). Some sample steps in the image preparation are illustrated in **Error! Reference source not found.**. The figure includes the original image, the image after step 4, and the LSM after step 5.

(1) P5, L19: "Some sample steps…" Why not all? Which steps are not shown?
(2) Addressed as highlighted above.

(1) P5, L26: What is the reason for this the colour balance drift?

(2) The color response of every camera sensor is different, even for cameras of exactly the same type. No two TSI cameras report exactly the same color values for clear blue sky, for example. In addition, camera sensors age with use. Most CCD and CMOS sensors will change their sensitivity over time, perhaps due to defect accumulation as they are exposed hundreds of thousands of times, sometimes to extreme sun (shadow-strip malfunctions do occur and are present in the TSI record), and as the cameras exist in extreme temperature conditions. Revised the statement and inserted reference.

(3) Pg 6, ln 13: Since the algorithm is intended for multiple TSI locations and records taken over long time, including device changes, it is necessary to consider the fact that no two camera devices have exactly the same colour response, even if of same type (Ilie and Welch, 2005).

(1) P6, L3: Please specify "from across all TSI records available to the authors". Is this a good reference if the TSI white balance generally drifts? Another possible

method would be to calibrate against a white or gray point in the images (e.g. bright cumulus clouds).

(2) I changed the sentence for clarity. Clear sky near zenith is a good reference. The drift is very slow, and a check-back is needed less than once a year, unless the actual device changed. A device change is a bigger influence on colour changes than the aging of the sensors, although these also influence the tinting. One can not colour-check against white, since the relationships between the different colour channels gets lost if all channels are saturated. Gray values exist in nature in so many different contexts and variations that finding a standard is not easily possible. However, a clear high-pressure sky, near zenith and not close to the sun itself provides a reproducible reference.

(3) Pg 6, ln 22ff: The reference values are based on colour values for clear sky images from the TSI records listed in Table 1. Near-zenith, clear blue sky provides a reproducible colour reference in all the locations.

---

(1) P6, L4: The method how the TSI images were corrected using the scaling factors is not quite clear. It seems like only the blue channel (B) is corrected? How is the normalization of the brightness between 0 and 255 ensured?

(2) The paragraph discussing the tint adjustment has experienced editing, based on both reviewer's comments, and reads now:

(3) Once these colour-scaling factors are determined for a series, every image was then tinted by generating an average colour $(\overline{B}, \overline{G}, \overline{R})$ for a small near-zenith sky-sample and applying

$$B' = \left[B + \alpha\left(\beta_B \overline{B} - B\right)\right]$$
$$G' = \left[G + \alpha\left(\beta_G \overline{G} - G\right)\right]$$
$$R' = \left[B + \alpha\left(\beta_R \overline{R} - R\right)\right]$$

$$(4) \qquad (8)$$

to each colour channel and pixel, respectively, followed by a simple scaling to preserve the total brightness of the pixel $I = \sqrt{B^2 + G^2 + R^2}$. For the series SGP 2018, these factors were β = (0.9, 0.78, 1) and α=0.4. The coefficient α regulates the strength of the tinting such that α=0 leads to no tint, and α=1 produces an image of a single colour. This tinting is minimal, and linear colour behaviour is a reasonable assumption.

---

(1) Please define R, G, B. Is this the brightness of the respective color channel?

(2) Correct. Language to this extend was inserted on page 6 line 15.

(3) Pg 6, line 15: Every pixel in a TSI image exhibits a value between 0 and 255 for each of the three colour channels blue (B), green (G), and red (R). The colour values represent the intensity of the colour channel registered for the particular pixel, varying between 0 (no intensity) and 255 (brightest possible).

(1) P6, L9: "The second step identifies the horizon circle, stretches the visible horizon ellipse…", circle or ellipse? L21 states that the coordinate transformation corrects for deviations from a circle for the 22▯ halo. And thus also for the horizon?

(2) While the mirror is circular, a slight misalignment of mirror and camera axis can make the circle appear stretched into an ellipse. This is detrimental to the plan to identify the solar position from time and coordinates, and must be corrected. The paragraph for step (2) was reworded thus:

(3) Pg 7 line 2 ff: Step (2) is a stretch-and-shift process that identifies the horizon circle. Occasionally, a slight misalignment of camera and mirror axis leads to an elliptical appearance of the sky image. A calibration is necessary in such cases to stretch the visible horizon ellipse to circular shape, and to centre the horizon circle as close to the zenith as possible. A north-south alignment correction may also have to be applied. Both calibrations will ensure successful identification of the solar position in the next step. These calibrations become necessary if the TSI was not perfectly aligned in the field and need to be readjusted after any disturbances occurred to the instrument, such as storms, snow, instrument maintenance, etc. Typically, this can be once every few months, or sometimes several times per month. It is important to check the calibrations regularly by sampling whether the solar position was correctly identified after calibration.

---

(1) P6, L10: "A north-south alignment correction may also have to be applied." Was it applied? If not, the position of the sun and the 22▯ halo will be shifted. Please discuss.

(2) That was explained in the previous comment and revision. If an alignment was necessary it was applied. If it was not necessary, then it was not applied. It changes, as described above, sometimes weekly, sometimes only once or twice a year. It has no bearing on the halo and sun position if done correctly. These operations only serve to provide a good reference frame to determine the sun position in the images.

---

(1) P6, L11: "In addition, the horizon is chosen at a zenith angle smaller than 90▯, often between 85▯ and 79▯…" How often? Which threshold was used in the other cases? Does it affect the Local Sky Map anyway?

(2) These are details that have no bearing on the construction of the LSM, only on the position of the horizon circle, outside of which everything will be masked. As described above in answer to the resolution question, a pixel located in a TSI image close to the horizon (zenith angle 79°) covers a radial angular extend of more than 1.2 degree worth of zenith angle. The vertical resolution is so low that there is basically no informational value along the rim of the horizon. Blocking out these pixels does not influence the working of the algorithm. The text in the paragraph has been changed to:

(3) Pg 7, ln 10: In addition, the horizon circle is placed at a zenith angle smaller than 90°, often between 85° and 79°, to eliminate the strong view distortion close to the horizon, and in some cases, objects present in the view. As explained earlier, the zenith angle resolution per pixel exceeds 1.2° close to the horizon. The

information value for zenith angles larger than 80° is diminished. These pixels should be excluded from the analysis. Practically, this is a very thin ring cut from the original image but does help eliminate false signals from low sun angles. The current process requires to find these calibrations for a ~~handful~~ sampling of images in a series, and ==to== then apply them to all images in the series.

---

(1) P6, L19-21: How exactly was the image distortion investigated? Please support this statement by numbers.

(2) While indeed, the influence of the mirror on perspective was tested, inserting a section on optical transformations on a spherical mirrors, and the respective numerical solution, plus conclusion that it does not have an influence … it just seems excessive. Instead, we'll remove the reference to the mirror distortion, and refer to previous publications (Long et al) on perspective treatment in TSI images.

(3) Page 7, line17ff: Step (3) removes the perspective distortion. The projection of the sky onto the plain of an image introduces a perspective distortion, as described in Long et al (Long et al., 2006). A coordinate transformation is performed to represent the sky in terms of azimuth and zenith angles. The azimuth is the same in both projections. Zenith angle θ relates to the radial distance r in the original image from the centre of the horizon circle as $r = R \sin \theta$. While R is not determined, image horizon radius R_H and horizon zenith angle θ_H provide one known point to allow for proportional scaling. The coordinate transformation represents the sky circle in a way in which radial distance from zenith s_z scales with zenith angular coordinate θ as

$$s_z = \frac{R_H}{\sin \theta_H} \times \theta$$

~~We tested the influence of the spherical mirror reflection on the distortion. For camera positions at height h above a convex mirror of radius A where~~ $h/A \approx 1$, ~~the assumption~~ $\theta \sim s_{\bar{z}}$ ~~is reasonable.~~ One of the visible effects of this transformation concerns 22° halos: in the original TSI image, a halo appears as a horizontal ellipse; after the transformation it will have a shape closer to a circle.

---

(1) P6, L24: Which "extraneous details" are masked? Please specify.

(2) As below:

(3) Pg 7, ln 22: Extraneous details, such as the shadow strip, the area outside the horizon circle, the camera, and the camera mount, are masked.

---

(1) P6, L26: What are 40 sky degrees?

P6, L26: "Units of measurements in the LSM…". Why not simply use pixels? Or zenith and azimuth angles in degrees?

P6, L28/29: Do you refer to image distortion? "requiring an additional horizontal compression", please explain the procedure. "The algorithm is robust enough to allow this scaling by solar position alone, without loss of efficacy". This should be discussed together with the results.

(2) I will address these three comments together, since all of them relate to a fundamental misunderstanding of what LSM units are. I hope that the rewrite does help clarify the questions.

(3) Pg 7, 31ff In step (5), the standardized local sky map (LSM) is created. A sketch of the layout of the LSM is provided in Figure 1. The LSM provides a standard sky section, centred at the sun, oriented with the horizon at the bottom, and presented in the same units for all possible TSI images (independent on the resolution of the original). Units of measurement in the LSM are closely related to angular degrees, but do not match perfectly due to a zenith-angle dependence of the azimuth arc length. The LSM is generated by rotating and cropping the image from step (4) to approximately within 40° of the sun, with the sun at its centre. The side length of the LSM in pixels scales with the previously determined horizon radius R_H in pixels and the corresponding maximum zenith angle θ_H in ° as

$$w_{LSM}(pixels) = \frac{R_H(pixels)}{\theta_H(degrees)} \times 40°$$

(9)

Equation (9) provides a unit transformation between pixel positions and LSM units. For a TSI image of size 480×640 pixels, the LSM will have a size of approximately 240×240 pixels. For the earlier, smaller TSI images, the LSM has a size of approximately 140×140 pixels. The unit scaling includes the calibration choices R_H and θ_H, hence there is a slight variation in LSM pixel sizes. We eliminate the influence of the varying pixel sizes by performing all algorithm operations in standardized LSM units, which roughly correspond to angles of 1°. In other words, all LSM are equivalent to each other in terms of their LSM units, but not in terms of pixel positions. At θ=45°, the arc length of azimuth angle φ is equivalent to the arc length of θ of same size; however, if θ>45° the azimuth arc is stretched, requiring an additional horizontal compression to ensure equivalence of horizontal and vertical angular units. ~~The algorithm is robust enough to allow this scaling by solar position alone, without loss of efficacy.~~ The LSM is divided into quadrants, shown in Figure 2, which are analysed and classified separately by the algorithm described in the next section.

---

(1) Figure 2: Please include a figure showing the LSM as an overlay to the TSI image with 22 · halo of Fig. 1 in addition. It would be very helpful to see which portion of the image is actually used for the analysis of the 22 · halo when it comes to interpreting the results.

(2) In fact, the LSM in figure 2 IS an overlay of the exact thing proposed here. The purpose of figure 2 IS to show which portions of the image are used for analysis, and to support the definition of the variables used. The caption was edited in response to reviewer 1. The halo appears at 21 LSM units, as can be ascertained from the text as well as from the data in figure 3. I included a sketch of the halo in the figure in the hope this makes this easier to understand.
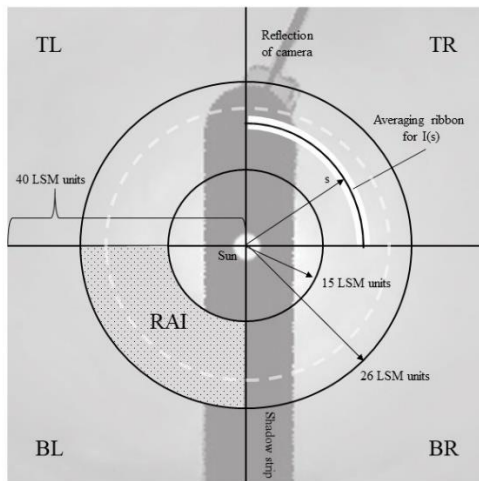
(3)

Figure 1. Layout of the local sky map (LSM). The LSM is divided into four quadrants, named according to their position as TR – top right, BR – bottom right, BL – bottom left, and TL – top left. The RAI is the Radial Analysis Interval for which STS and IHS properties are evaluated. The approximate position of the halo maximum is sketched in light grey. **Shadow strip and camera are excluded from analysis.**

2.3 Computing Sky Type and Halo Properties
2.3.1 Average radial intensity (ARI)

(1) · P7, L5/6: "We found it useful…", as in previous publications (e.g. Forster et al. 2017). It is indeed practical to use the radial brightness distribution since for randomly oriented ice crystals (causing the 22 · halo) the scattering phase function varies only along the scattering angle.

(2) I met Linda Forster at the Gordon Conference on Radiation and Climate in 2015. We both presented posters on halo identification in images, and both independently have used the radial brightness gradient as access. I mention this since the reviewer repeatedly appears to allude that this approach must be referenced to Forster et al. while in truth it is a common-sense approach, independently used in our algorithms. This comment requires no change in the text at this position. Reference to the work of Forster has been made in various other locations throughout the manuscript.

---

(1) P7, L14/15: move this explanation of the LSM to section 2.2

(2) The comment "The LSM is divided into four quadrants: TR = top right, BR = bottom right, BL = bottom left, TL = top left, analysed separately, and then recombined for the image scores." Has now moved to pg 8 line 31. Since language referring to the quadrants has been inserted into section2, I will leave this in place to allow the discussion that follows in the text.

---

(1) P7, L19/20: How does a radial average over 4 pixels affect the visibility of the 22 ˙ halo? Is it necessary? Does the angular resolution of 0.4 ˙ to 0.7 ˙ , as stated in L25, still hold after averaging?

(2) This is an excellent question, and answering it helps to improve the text. Earlier, the text was expanded to include more detailed information on the resolution. The resolution varies across the sky, with 0.4° close to zenith angles of 45°, but only 1.3° close to zenith in declination, and 1.3° in azimuth close to horizon. The averaging mostly addresses the noise of averaging a circle in a coarse square grid. By allowing a band instead of a sharp line, a continuous circular band is averaged, instead of a broken series of squares (pixels) that align somewhere close to a perfect circular line. The averaging does not diminish the appearance of the halo signal (see figure 3, panel B on the left). However, it improves the smoothness of the curve $\eta(s)$ which in turn makes it easier to write an algorithm to find maxima, minima, slopes along an imperfect series of data. Perhaps, the insertion of the following line provides clarification:

(3) Pg 9, ln 4 ff: ..Due to the low resolution of the LSM, and due to some noise in the data, we average *I(s)* over a circular ribbon with a width of 4 pixels, centred at *s*. Computing *I(s)* over a thin ribbon addresses issues encountered when averaging over a circle in a coarse square grid, allowing continuity where otherwise pixilation may interrupt the line of the circle. Figure 2 shows..

---

(1) P7, L3: Please define "a"
(2) I changed the presentation of the equation for the running average instead. The "a" is not a parameter of consequence, only indexes the terms included in the running average.
(3) Pg 9 , ln 10 $\overline{I}_6(s) = \frac{1}{N} \sum_{s-3LSMunits}^{s+3LSMunits} I(s)$

(10)

---

(1) P7, L24: Please indicate the position of the 22 ˙ halo in Fig. 3 ˙ P7, L27:

(2) Change in figure and caption for figure 3 was done.

(3) **Figure 2 Average radial intensity of the red channel is shown versus radial distance s, measured in LSM units, for the two images of** Error! Reference source not found.**, halo at left. Panel (A) includes the average intensity $I(s)$, a linear fit, and the running average $\overline{I}_6(s)$ as averaged over a width of 6 LSM units. (B) shows the radial intensity deviation $\eta(s)$. The halo signal is visible as a minimum at 17 LSM units, followed by a maximum at 21 LSM units in the left column.**

(1) What is 15-26 LSM units in degrees? Where is the 22 · halo in terms of LSM units? · Could be visible in an additional figure with an overlay of the LSM onto the TSI image with 22 · halo of Fig. 1 (as suggested above)

(2) As addressed above. LSM units are roughly equivalent to sky degrees, but not perfectly. Halos appear between 21 and 22 LSM units. Colours can not be resolved.

2.3.2 Sky type score (STS)

(1) P8, L3: Please provide the exact number of images/image segments that were used for training, cf. P10, L22: 44026 images?

(2) This information is already contained in the text of the section. The formulation of STS properties is based on 80 seed images.

The number the reviewer cites refers to the number of records contained in SGP March 2018, later used to test and train the algorithm. However, this particular position in the text does not address this later testing and training.

(3) Properties of *I(s)* were computed for the set of 80 seed images mentioned in section **Error! Reference source not found.**. Twenty images for each sky type were divided further by sky quadrants, yielding between 60 and 80 property sets for each sky type to seed the master table. Some quadrants were eliminated by horizon-near solar positions.

(1) P8, L16: How about introducing the metrics defined in section 2.1 here? In my opinion, the procedure is much easier to understand after the "properties" are explained. In section 2.1 it would be sufficient to explain that a multivariate analysis is performed based on image features/properties. The TSI images are then classified by comparing these features to reference values in a look-up table.

(2) Thank you for this suggestion. We have considered this before. However, since there are two separate sections making use of the same approach, only differing in details, we decided at the time to present this in the form you read. The proposed re-arrangement may be considered again if the journal decides to move forward with publication.

The master table does not really fit the term "look-up" table. The means and covariances are read by the program exactly once, at the beginning. The term "look-up" table implies repeated referencing to a database, and that is not what is occurring here.

(1) **P8, L17: "continually refined master table"** ☐ **Please explain this procedure.**

(2) This is done later, in section 3, and does not need to be said here. Eliminated the wording.

(3) **Pg10, ln6 The ~~continually refined~~ master table defines a mean value vector *M*,**

(1) P8, L18/19: As suggested above it would be more convenient for the reader to define Eq.3 here.

(2) For now, I will leave the structure as is, and reconsider if asked for a final version of the manuscript. Again, Equation (3) (now 2-6) is used in multiple independent formulations of the same algorithm. It really only needs to be included once, and then referenced.

---

(1) P8, L19: Please provide the range of values expected for F_{image} (in case of "22 · halo" and "no 22 · halo"). This might already be interesting to note on P5, L7.

(2) This comment refers to a position in the section on sky type scores, not halo scores. No halo decisions are made here. The values for F are arbitrary, due to the choice of C. The relative values matter for decisions on sky type, as already explained in the text pg10 lns10-20.

---

(1) P8, L25: How was the threshold of 10_{-8} chosen? Is it simply outside of the range of F? What kind of images yield this result? · explained later on P12, L1-3. Should be already mentioned here.

(2) Inserted additional sentence.

(3) **Pg10, line 18.** Such conditions may include overexposed images, horizon-near solar positions, a bird sitting on the mirror, and other conditions that produce images very different from the sky types sought after.

---

(1) P8, L29: "taken for the combined sky" · "for all 4 LSM quadrants"?

(2) Corrected.

(3) Pg10 line23 ~~taken for the combined sky~~ taken for all 4 LSM quadrants combined.

---

(1) P9, L9: Please explain the challenges that can be addressed by the "radial scattering analysis" and how

(2) Inserted sentence

(3) Page 11, line 1-3 The variation in radial intensity gradient as scatterers are present along the optical path can provide an alternative assessment for the presence of cirroform clouds, solving problems of classifying near-solar pixels using a colour ratio and/or intensity value only (Kennedy et al., 2016; N. Long et al., 2006).

2.2.3 Ice halo score (IHS)

(1) · P9, L9: The 22 · halo is formed by ice crystals in high-level cirrus clouds. So it is visible wherever cirrus clouds are present and not obstructed by low-level water clouds. The sentence as it stands now gives the wrong impression that the 22 · halo is overlaid over low-level clouds. Please correct the sentence accordingly.

(2) Corrected. Thanks.

(3) Pg11, line6: The 22° halo is a signal in the image that can be obscured by many other image features, including low clouds, partial clearings, inhomogeneous cirrostratus, regions of over-exposure, and near-horizon distortions.

---

(1) P9, L10/11: The fact that 22·halos are present in images classified as CLD and CLR provides more information about the definition of these categories and the selection of criteria rather than about the formation of the 22·halo. Please adjust the formulation of the sentence to avoid misunderstanding.

(2) This sentence is supposed to lay out the challenge of isolating the halo in a variety of sky conditions. Eliminated reference to algorithm sky types.

(3) Pg 11, line 7. The appearances of ice halos span a wide variety of sky conditions, ranging from almost clear skies to overcast altostratus skies, with the majority of halo phenomena appearing in cirrostratus skies.

---

(1) P9, L16: "variations in calibration" The image calibration should not vary across the images. The authors probably want to refer to the north-south mis-alignment of the camera and the coarse angular resolution which can pose a problem in identifying exact position of the 22·halo peak.

(2) True, no variation in the short term, however, as described in the rewritten section calibrations, sometimes recalibrations are necessary. The rewrite of section 2.1 addressed this.

---

(1) P9, L31: According to theory, the 22·halo peak should not be at the "same" location for the red and blue colour channel, but shifted. Is this feature used for the detection of 22·halos?

(2) No, this feature was not usable in these images. Resolution does not allow to distinguish the peak locations in a statistically reliable manner. In table 4, the peak locations are given together with their standard deviations. No significant difference can be gleaned from the color channels. A sentence was added.

(3) Pg12, line 1: The separation of colours observed in an ice halo display is not resolved with statistical significance in the TSI images, therefore this was not used as a criterion for halo detection.

---

(1) P10, L11: Please define "w" here, instead of L15.

(2) Inserted:

(3) Pg12, line 10: We added a Gaussian broadening to the time series of halo scores F_i, taken at times t_i with a broadening w

---

(1) Figure 5: Please provide values for the IHS at the y-axis of the lower panel
(2) Figure was revised accordingly.

---

(1) Is the IHS calculated for each quadrant separately? (How) are they combined to classify the image? · info on P10, L22 should be stated here as well as in section 2.3.2.
(2) This sentence was already contained in the text. It moved to the reference to figure 5.
(3) Pg12, line14: The raw halo score F is computed for the four quadrants of an individual image, their sum is used to assign the raw score for the whole image.

---

3 Results for January through April 2018

(1) · P10, L28: The values for $C = 10_6$ and w=3.5 (w=4 was defined in L15!) should be mentioned earlier, where the respective equations were defined. Eq. 2 should be Eq. 5?

(2) Both, C0 and w are arbitrarily chosen, and are passed as a parameter as befits the question. The reference to w=4 images is specific for the day data in figure 5. For the evaluation in section 3, w=3.5 minutes. This limits the time resolution for halo appearances to 3.5 minutes, but smooths out false halo singals encountered in the record for that month. The equation references have been corrected in the renumbering of equations.

---

(1) P10, L19: It is not be surprising that "high halo scores coincide with strong CS signals", however it can be considered a confirmation that the image features used to train the algorithm were reasonably selected.

(2) Yes.

---

(1) P10, L31 through P11, L2: The determination of a "cut-off" or threshold value "to assign an image with a label of halo/no halo" results from training the algorithm. The same way as the threshold of 50% for the sky type. In both cases the threshold is "arbitrary" to some extent, but should be chosen to minimize either false positive or false negative classifications. This is correctly stated later on P11, L19, but should be mentioned earlier.

(2) Clarifying phrase inserted. Also corrected the limit value to the one finally used in the computations.

(3) Page 13, line 14: Our testing, minimizing false negatives and maximizing correct positives, places it at around 4000 for the month of March.

---

(1) Table 5: The difference between "%vis" and "%alg" is not quite clear. It seems that "%vis" provides an assessment of the visual image classification? This might be confusing for the reader. The interesting quantities here are the fraction of correctly and incorrectly classified images by the algorithm, compared to the ground truth (visual classification). Note that IHS > 4000 in the caption, but IHS > 3500 in the text!

(2) The caption contains language explaining "%vis" and "%alg". It is still confusing, even to me. Adding an example to the caption. Number was corrected in text.

(3) Caption for table 5: Table 2. STS and IHS test results for SGP March 2018. Visual assignments were made iteratively in step with the algorithm results as described in section 3. Given are the percentages of images of visual type that have been assigned an algorithm type (%vis), and the percentages of the algorithm type that correspond to a visual type (%alg). For example, 88% of all visual CS skies are also classified as CS by the algorithm, but only 86% of all algorithm CS skies also identify as CS if inspected visually. Agreement combinations in bold. IHS > 4000 to count an algorithm halo.

---

(1) P11, L4: "A small percentage of visual CLD skies trigger a PCL signal, mostly due to inhomogeneities in cloud cover." Please provide a number for the percentage. Does CLD mean completely overcast? Or do the inhomogeneities here correspond to small clearsky patches?

(2) CLD means that the radial analysis area exhibits properties close to an overcast sky (positive or zero gradient, low values of intercept, color ratio near 1, etc). Since the sky types are assigned only in the radial analysis area of each quadrant, this is not a statement about the whole sky. The percentage is given in table 5, which it discussed in this spot in the text. The inhomogeneities refer to differences in grayness across the analysis area, triggering a high dispersion in intensity values.

(3) Pg13, line 15: In Table 2, visual and algorithm results of the sky type assignments are cross-listed. It is worth reminding the reader that sky types are assigned only for the radial analysis interval indicated in Figure 1. Cloudy skies are reliably identified by the algorithm. A small percentage (3%) of visual CLD skies trigger a PCL signal, mostly due to inhomogeneities in cloud cover.

---

(1) · P11, L4/5: Please provide a number stating how successful the classification of CLR is.

(2) As given in table 5. Inserted number also in text.

(3) Pg 13, line 18: The algorithm classifies 95% of all visual CLR skies correctly.

---

(1) P11, L27: If some CLR images were labeled as "22 ⋅ halo" why is the fraction of halo instances of CLR all sky type 0% in Tab. 5?

(2) This comment is confusing. Neither table 5 nor the location in the text refer to the stated issues. I will proceed under the following assumptions (1) the reviewer means table 6, (2) the reviewer refers to a now revised second sentence of sections 2.3.3 (?).
Table 6 lists that no halos where assigned in CLR skies, and that no CLR skies registered a halo signal. The second sentence in 2.3.3 was changed as listed above, to say that skies that appear clear can show a halo.

---

(1) P11, L23-31: The discussion of the challenges of visual classification of TSI images is very interesting, especially for other publications relying on this. As correctly mentioned, additional Lidar observations together with a temperature threshold e.g. from radiosonde data are useful to improve the classification (cf. Sassen et al. 2003 and Forster et al. 2017). Please add the respective citation also on P13, L7-9 and P13, L30.
(2) References added.
(3) Page 14, line 8ff: It is therefore a future necessity to combine the visual assignments of sky types with LIDAR data for altitude, optical thickness, and depolarization measurements to make an accurate assessment of the efficacy of the halo detection, following closely the processes described by Sassen et al. (Sassen et al., 2003) and Forster et al. (Forster et al., 2017).

---

(1) P12, L7: Please explain "various dimensions of the record".
On P10, L22 it was stated that "An image IHS and STS are assigned as the average over all scoring quadrants." How were the results for the individual quadrants obtained in Tab. 6?

(2) Changed sentence to:

(3) Pg 14, line 20: The ice halo statistics in **Error! Reference source not found.** lists data on ice halo statistics, including duration, number of incidents, and data on partial halos. The partial halo data are based on the individual quadrant IHS for an image, while the image score is used for duration and incidence information.

---

(1) It should be noted that due to the shadow band a "full 22 ⋅ halo" actually misses its top and bottom.
(2) I changed the designator in the table to 4/4 halo, to make clearer the connection to the number of halo-scoring quadrants.

(3) Table 6: 4⁄4 22° halo instead of "full 22° halo"

---

4 Summary

(1) · P13, L24: 86% vs 85% on P11, L18!
(2) Corrected the number
(3) Pg 16, line 13 The algorithm has been found to be about 90% in agreement with the visually assigned sky type, and 85% in agreement with the visually identified ice halo score.

---

(1) P13, L27/28: "The algorithm now will be applied to deliver ice halo data for the longterm TSI records accumulated in various geographical locations of ARM sites" Please replace by "In the future, the algorithm will be applied…" to avoid the misunderstanding that this was performed in the present study.
(2) Done.
(3) Page 16, line 16. In the future, the algorithm will be applied to deliver ice halo data for the long-term TSI records accumulated in various geographical locations of ARM sites, and allows further investigation into correlations with ...

Please consider the following remarks to further improve the quality of the manuscript:
The use of technical terms in the manuscript should be revised. In several instances a more commonly used expression exists, which should be used instead where applicable. For example:

(1) "Ice halo", I would suggest using the term "halo display", which is most commonly used in the literature. Please replace "ice halo" by "22 · halo" wherever this specific type of halo display is referred to, e.g. P1, L18 and P12, L10.
  IHS could be changed to HS22 or simply HS, when it is clear that it is only applied to the 22 · halo.

(2) I changed multiple instances where clarity was improved. The IHS designator arises from the software implementation of the algorithm, and will remain.

---

(1) "look-up table" might be a more commonly use term than "external expandable master table". It is not clear what "expandable" and "external" means in this context? Most tables are expandable.
(2) The term "look-up" table implies continued reference to a data base or external file while the algorithm is working. That is not the case. The terms expandable and external " already fell in the revisions. I think the term "master table" is closest to a reference file that produces the means and covariance matrices, and is read exactly once during algorithm execution.

…

(2) Many of the suggested improvements in this series were incorporated in the revised manuscript.

Typos and suggestions for improvement:

(2) All implemented as proposed, with the exception of "P8,L2 Consider starting with the explanation of the properties of I(s). It will make the rest of the section much easier to follow." Will reconsider if final version is requested.

Analysis Algorithm for Sky Type and Ice Halo Recognition in All-Sky Images

Sylke Boyd, Stephen Sorenson, Shelby Richard, Michelle King, Morton Greenslit

Division for Science and Mathematics, University of Minnesota-Morris, 500 E 4th Street, Morris, MN 5 *Correspondence to*: Sylke Boyd (sboyd@morris.umn.edu)

Abstract. Halo displays, in particular the 22⬚ halo, have been captured in long-time series of images obtained from Total Sky Imagers (TSI) at various Atmospheric Radiation Measurement (ARM) sites. Halo displays form if smooth-faced hexagonal ice crystals are present in the optical path. We describe an image analysis algorithm for long-time series of TSI images which identifies images with 22⬚ halos. Each image is assigned an ice halo score (IHS) for 22⬚ halos, as well as a sky type score

10 (STS), which differentiates cirrostratus (CS), partially cloudy (PCL), cloudy (CLD), or clear (CLR) within a near-solar analysis area. The colour-resolved radial brightness behaviour of the near-solar region is used to define the characteristic property spaces used for STS and IHS. The scoring is based on distance from a region in that property space, using tools of multivariate Gaussian analysis. A ~~n external expandable master~~ master table of characteristic properties allows continued training of the algorithm. Scores are assigned to the standardized sun-centred image produced from the raw TSI image after a series of

15 calibrations, rotation, and coordinate transformation. We present test results on halo observations and sky type for the first four months of the year 2018, for TSI images obtained at the Southern Great Plains (SGP) ARM site. A detailed comparison of visual and algorithm scores for the month of March 2018 shows that the algorithm is about 90% reliable in discriminating the four sky types, and identifies 86% of all visual halos correctly. Numerous instances of halo appearances were identified for the period January through April 2018, with persistence times between 5 and 220 minutes. Varying by month, we found 20 that between 9% and 22% of cirrostratus skies exhibited a full or partial 22⬚ halo.

Introduction

Modelling and predicting the Earth's climate is a challenge for physical science, even more so in light of the already observable changes in Earth's climate system (Fasullo and Balmaseda, 2014; Fasullo et al., 2016; IPCC, 2013, 2014). Global circulation

25 models (GCMs) describe the atmosphere in terms of a radiative dynamic equilibrium. The Earth receives solar shortwave (SW) radiation and discards energy back into space in form of terrestrial long-wave (LW) radiation. The radiation balance of the earth has been subject to much study and discussion (Fasullo and Balmaseda, 2014; Fasullo and Kiehl, 2009; Kandel and Viollier, 2010; Trenberth et al., 2015). Global Circulation Models (GCMs) describe the influence of various parts of the earth system in terms of radiative forcing factors (Kandel and Viollier, 2010; Kollias et al., 2007). Clouds may restrict the SW flux

reaching the surface, but they also influence the LW emissions back into space. While low stratus and cumulus clouds exhibit a net negative radiative forcing, high cirroform clouds are more varied in their radiative response, varying between negative and positive forcing depending on time of day, season, and

5 geographical location (Campbell et al., 2016). The Fifth Assessment Report from the IPCC in 2013 (IPCC, 2013) identified ice and mixed clouds as major contributors to the low confidence level into the aerosol/cloud radiative forcing. The uncertainty in the aerosol/cloud forcing has implications for the confidence in and for the variance of the predictions of global circulation models (Fu et al.,

10 2002; Trenberth et al., 2015). Closing the radiation budget of the Earth hinges on reliable cloud data (Hammer et al., 2017; Schwartz et al., 2014; van Diedenhoven et al., 2015; Waliser et al., 2009). Traditionally, cloud radiative forcing is modelled using a cloud fraction based on sky images (Kennedy et al., 2016; Kollias et al., 2007; Schwartz et al., 2014). Cirrostratus clouds, lacking sharp

15 outlines, pose a challenge to this approach (Schwartz et al., 2014). The uncertainty about the role of cirrus in the global energy balance has been attributed to limited observational data concerning their ~~composition, and~~ temporal and spatial distribution as well as their microphysics (Waliser et al., 2009). Cirroform clouds, at altitudes between 5000-12,000 m, are effective LW

20 absorbers. Cloud particle sizes can range from a few microns to even centimetre sizes (Cziczo and Froyd, 2014; Heymsfield et al., 2013). Methods to probe cirrus cloud particles directly involve aircraft sampling (Heymsfield et al., 2013) and mountainside observations (Hammer et al., 2015). Ground- and satellite-based indirect radar and LIDAR measurements (Hammer et al., 2015; Hong et al., 2016;

25 Tian et al., 2010) give reliable data on altitudes, optical depths, and particle phase. Even combined, these methods leave gaps in the data for ~~in our knowledge of~~ spatial and temporal composition of ice clouds. The analysis of halo displays as captured by long-term total sky imagers may provide further insight and allow to close some of the gaps.

34

30 Optical scattering behaviour is influenced by the types of ice particles, which may be present in very many forms, including crystalline hexagonal habits in form of plates, pencils and prisms, hollow columns, bullets and bullet rosettes, and amorphous ice pellets, fragments, rimed crystals and others (Bailey and Hallett, 2009; Baran, 2009; Yang et al., 2015). Only ice particles with a simple crystal habit

35 and smooth surfaces can lead to halo displays (Um and McFarquhar, 2015; van Diedenhoven, 2014). Usually, this will be the hexagonal prism habit, which we can find in plates, columns, bullet rosettes, pencil crystals, etc. If no preferred orientation exists, a clear tell-tale sign for their presence is the 22□ halo around a light source in the sky, usually sun or moon. More symmetry in the particle

40 orientations will add additional halo display features such as parhelia, upper tangent arc, circumscribed halo, and others (Greenler, 1980; Tape and Moilanen, 2006). As shown in theoretical studies (van Diedenhoven, 2014; Yang et al., 2015), halos form in particular if the ice crystals exhibit smooth surfaces. In that case, the forward scattered intensity is much more pronounced as in cases of rough

45 surfaces, even if a crystal habit is present. If many of the ice particles are amorphous in nature, or did not form under conditions of crystal growth- for example by freezing from super-cooled droplets, or by riming – the forward scattering pattern will be weaker, and similar to what we see for liquid droplets: a white scattering disk surrounding the sun, but no halo. In turn, roughness and

50 asymmetry of ice crystals influence the magnitude of backscattered solar radiation, thus influencing the radiative effect of cirrus clouds (van Diedenhoven, 2016). If the particles in the cirroform cloud are very small, e.g. a few microns (Sassen, 1991), diffraction will lead to a corona. Hence, wWe believe that a systematic observation of the optical scattering properties adds information to

55 our data on cirrus microphysics composition and cirrus radiative properties. The authors observed the sky at the University of Minnesota Morris, using an all sky camera, through a five-month period in 2015, and found an abundance of halo

features. There are a few studies pursuing a similar line of inquiry (Forster et al., 2017; Sassen et al., 2003).

60   The study by Sassen et al (Sassen et al., 2003) showed a prevalence of the 22☐ halo, full in 6% and partial in 37.3% of cirrus periods, based on a ten-year photographic and LIDAR record of mid-latitude cirrus clouds, also providing data on parhelia, upper tangent arcs, and other halo display features, as well as coronas. The photographic record was taken in Utah, and based on 20-minute
65   observation intervals; cirrus identification was supported by LIDAR. The authors found an interesting ~~geographical~~ variability in halo displays, related to geographical air mass origin, and suggest that optical displays may serve as tracers of the cloud microphysics involved. Forster *et al.* (Forster et al., 2017) used a sun-tracking camera system to observe halo display details over the
70   course of several months in Munich, Germany, and a multi-week campaign in the Netherlands in November 2014. A carefully calibrated camera system provided high-resolution images, for which a halo detection algorithm was presented, based on a decision tree and random forest classifiers. Ceilometer data and cloud temperature measurements from radiosonde measurements
75   were used to identify cirrus clouds. The authors report 25% of all cirrus clouds also produced halo displays, in particular in the sky segments located above the sun. The fraction of smooth crystals necessary for halo display appearance is at a minimum 10% for columns, and 40% for plates, based on an analysis of scattering phase functions for single scattering events (van Diedenhoven, 2014). While this
80   establishes a lower boundary, it is correct to say that the observability of a halo display allows to conclude that smooth crystalline ice particles are present and single-scattering events dominate. The consideration of the percentage of cirrus clouds that display optical halo features allows therefore, upon further study, inferences about the microphysical properties of the cloud. This raises interest in
85   examining existing long-term records of sky images.

36

Long-term records of sky images have been accumulated in multiple global sites. The Office of Science in the US Department of Energy has maintained Atmospheric Radiation Measurement (ARM) sites. These sites, among other instruments, contain a Total Sky Imager (TSI), and have produced multi-year

90   records of sky images. In this paper, we introduce a computational method to analyse these long-term records for the presence of halo displays in the images. We are introducing an algorithm to analyse long sequences of TSI data, and produce a time record of near-solar sky type, differentiated as cirrostratus (CS), partly cloudy (PCL), cloudy (CLD), and clear (CLR) sky types, as well as assign an ice

95   halo score (IHS). The resolution and distortion of the TSI images restricts the halo search to the common 22☐ halo. Other halo features, such as parhelia, can occasionally be seen in a TSI image, but often are too weak or too small to reliably discriminate them from clouds and other features. Coronas are obscured by the shadow strip, and often also by over-exposure in the near-solar area of the

100   image. The algorithm offers an efficient method of finding 22☐ halo incidences, full or partial. Since ARM sites also have collected records of LIDAR and radiometric data, the TSI halo algorithm is intended to be compared to other instrumental records from the same locations and times. This will be addressed in future work.

105   Section 1 describes the TSI data used in this work. Section 2 presents the details of the image analysis algorithm, including subsections on algorithm goals, image preparation, and sky type and halo scoring. Section 3 applies the algorithm to the TSI

data record of the first four months of 2018, and examines effectiveness and types of data available for this interval. Summary and outlook are given in Sect.~~ion~~ 4.

1 TSI images

Images used in this paper w~~h~~ere obtained from Atmospheric Research Measurement (ARM) Climate Research Facilities in

5 three different locations: Eastern North Atlantic (ENA) Graciosa Island, Azores, Portugal; North Slope Alaska (NSA) Central Facility, Barrow AK; and Southern Great Plains (SGP) Central Facility, Lamont, OK (ENA, 2018; OLI, 2018; SGP, 2018). The ranges and dates vary by location, as listed in Table 1. The images were taken with Total Sky Imagers, which consist of a camera directed downward toward a convex mirror to view the whole sky from zenith to horizon. A sun-tracking shadow band is used to block the sun, which covers a strip of sky from zenith to horizon. Images were recorded every 30 seconds. The longest series was

10 taken at the Southern Great Plains (SGP) location, reaching back to July 2000. The images, in JPEG format, have been taken continuously during day time. Aside from night time and polar night, there are some additional gaps in the data, perhaps due to instrument failure or other causes. Camera quality, exposure, image resolution, and image orientation varies over time as well as by location. ~~The angular resolution varies with zenith angle but can rise above 0.7 □ for the smaller images (0.4□ for the larger size), in particular for sky sections close to the horizon.~~ For example, an image from SGP taken in 2018 has a size of 488 by 640 pixels. The

15 short dimension limits the radius of the view circle to at most 240 pixels. A pixel close to the center of the view circle corresponds to an angular sky section 2.8° wide and 0.24° tall. At SGP, the solar position never reaches this point. Close to the horizon, one pixels averages a sky section that is 0.24° wide and 1.24° tall. Best resolution is achieved at zenith angle 45°, in which case every pixel represents a sky region of 0.33° by 0.33°. The image distortion is largest for sky segments close to the horizon due to perspective distortions of the sky. We used a sampling of eighty images taken from

across the TSI record and across all available years to

38

20 <mark>define and train the algorithm</mark> (ENA, 2018; NSA, 2018; SGP, 2018). This included images

visually identified as CS, PCL, CLD, CLR, and halo-bearing. <u>Descriptions of these sky types are provided in</u> Table 2. The 80

sample images The 80 samples were used to develop the algorithm and define a suitable set of characteristic properties for STS

and IHS. This set will be referred to as seed images since they also initialize the master table described below.

2 Algorithm

25 **2.1 Goal and Strategy**

The algorithm aims to process very large numbers of images, and return information about the presence of 22☐ halos, as well as the general sky conditions. The program is written in C++ and uses the opencv library for image processing. If given a list of image directories, the algorithm proceeds to sequentially import, process, and score TSI images resulting in a sky type score (STS) and an ice halo score (IHS). In order to discriminate the sky types listed in Table 2, for example, or to single out the relatively weak halo signature from an image we use a multivariate Gaussian analysis. This begins with the definition of a set of N_P properties of the image, selected to be characteristic for a sky type or a halo. Let this set of properties be a vector

$$X = \{x_i\}_i^{N_P}$$

5 <mark>(1)</mark>

A master table is created from N_{master} images that visually exhibit the target feature, i.e. a halo or a clear sky. This set defines an ellipsoidal region in the property space of X. The region is centred at the vector of mean values

39

10

$$M=\{\mu_i\}_{Ni=P1}$$

$$=\frac{1}{N_{master}}\sum_{k=1}^{N_{master}} \mu_i x_{ik}$$ (2)

The stochastic ellipsoid is described by the N_P $\square$ (3)
N_P covariance matrix

$$\Sigma=(X-M)(X-M)^T=\begin{pmatrix}\sigma_{11} & \sigma_{12} & ... \\ \sigma_{21} & \sigma_{22} & ... \\ ... & ... & ...\end{pmatrix}$$

15 (4) evaluated for the sets in the master table. The elements of the
covariance matrix are computed as

$$\sigma_{ij} x_{ik} x_{jk}-\mu_i\mu_j \qquad =\frac{1}{N_{master}}\sum_{k=1}^{N_{master}}$$

20 (5)

The property vector of any further image X_{image} will then be referenced with M
and $\square$ in form of a multivariate normal distribution

25 $$F_{image}=C_0 exp\left(-\frac{1}{2}(X_{image}-M)_T\Sigma_{-1}(X_{image}-M)\right)$$

$$(6)$$

in which the exponent is known as the square of the Mahalanobis distance in property space. The closer an image places to the region of interest, the higher its score will be. For the image properties we chose in STS and IHS computation, the elements of X_{image} lie within one order of magnitude of each other. Hence, no weighing became necessary for this application. In order to score a time series of property vectors X_{image}, one only needs to import M and $\square^{-1}$ once at the start of the analysis run. Both, 30 M and $\square^{-1}$, are computed a priori in a master table via Equations. (2) and (4). We are using a flexible spreadsheet for this purpose, allowing the addition of reference property vectors as more images are analysed. This allows to continually train the algorithm toward improvement of scoring. The pre-factor C_0 in Equation Eq. (6) is chosen later to place the values for F into a convenient number range. The algorithm is outlined in **Error! Reference source not found.**, together with the respective references to place in the text in which the steps are described. The details of STS and IHS will be treated separately below as

5   well. This basic algorithm structure is used on a standardised local sky map, described in 2.2. The details of STS and IHS will be treated separately below as well.

The code and accessories can be accessed at a GitHub repository (Boyd et al., 2018).

2.2 Image preparations and local sky map (LSM)

The goal of the image preparation is to create a local sky map centred at the sun, in easy-to-use coordinates, after a minimal 10 colour calibration, and after extraneous image parts have been masked. The image preparations include the following steps: (1) a colour correction, (2) an alignment calibration, (3) a removal of the perspective distortion, (4) masking and marking of the solar position, and (5)

rotation and crop to create a Local Sky Map (LSM). Some sample steps in the image preparation are illustrated in ~~Figure 1~~Fig. 2, ~~. The figure includes~~ including the original image, the image after preparation step (4), and the

LSM after preparation step (5). The two sample images in Fig. 2~~The images~~ were taken at the Southern Great Plains ARM site

15 in March and April of 2018 (SGP, 2018). One of the images contains a solar 22° halo, the other one is a partly cloudy sky without any halo indications.

Step (1) is a colour correction. Both original images in ~~Figure 1~~Fig. 2 have a slightly green tinge, which is typical for images from the TSI at this location, in particular after an instrument update in 2010. This is noticeable in particular if images are compared to earlier TSI data from the same location, and can become a problem for the planned analysis, in particular for the

20 use of relative colour values. Since the algorithm is intended for multiple TSI locations and records taken over long time, including device changes, it is necessary to consider the fact that no two camera devices have exactly the same colour response, even if of same type (Ilie and Welch, 2005). The colour calibration used in this algorithm is based on sampling of clear-sky colour channels to define weighed scaling factors for a whole series of images. Every pixel in a TSI image exhibits a value between 0 and 255 for each of the three colour channels blue (B), green (G), and red (R). The colour values represent the

25 intensity of the colour channel registered for the particular pixel, varying between 0 (no intensity) and 255 (brightest possible). In a discoloured series, measurements of BGR were taken in clear-sky images (indexed CLR), and a scaling factor and weight for each colour channel defined based on this information:

$$\beta_B = 1.00$$

$$\beta_G = G_{ref} B_{CLR}$$
$$\times$$
$$G_{CLR} \cancel{B_{ref}} \; \cancel{\text{with}} \quad (B_{ref}, G_{ref}, R_{ref}) = (180,120,85)$$

$$\beta_R = \cancel{R_{ref}} \; B_{\cancel{CLR}}$$
$$\times$$
$$R_{CLR} B_{ref}\}$$

$$(7)$$

The reference values are based on colour values for clear sky images from the TSI records listed in Table 1~~Table 1~~. Near-zenith, clear blue sky provides a reproducible colour reference in all the locations. Once these colour-scaling factors are determined for a series, every image was then tinted by generating an average colour $(\bar{B}, \bar{G}, \bar{R})$ for a small near-zenith sky-

5   sample and applying

$$B' = \left[B + \alpha\left(\beta_B \bar{B} - B\right)\right]$$
$$G' = \left[G + \alpha\left(\beta_G \bar{G} - G\right)\right]$$
$$R' = \left[B + \alpha\left(\beta_R \bar{R} - R\right)\right]$$

$$(8)$$

to each colour channel and pixel, respectively, followed by a simple scaling to preserve the total brightness of the pixel $I = \sqrt{B^2 + G^2 + R^2}$. For the series SGP 2018, these factors were $\beta = (0.9, 0.78, 1)$ and $\alpha=0.4$. The coefficient α regulates the

10   strength of the tinting such that $\alpha=0$ leads to no tint, and $\alpha=1$ produces an image of a single colour. This tinting is minimal, and linear colour behaviour is a reasonable assumption.

Step (2) is a stretch-and-shift process that identifies the horizon circle. Occasionally, a slight misalignment of camera and mirror axis leads to an elliptical appearance of the sky image. A calibration is necessary in such cases to stretch the visible horizon ellipse to circular shape, and to centre the horizon circle as close to the zenith as possible. A north-south alignment

15   correction may also have to be applied. Both calibrations will ensure successful identification of the solar position in the next step. These calibrations become necessary if the TSI was not perfectly aligned in the field. They ~~and~~ need to be readjusted after any disturbances occurred to the instrument, such as storms, snow, instrument maintenance, etc. Typically, this can be once every few months, or sometimes several times per month. It is important to check the calibrations regularly by sampling across the series whether the solar position was correctly identified after calibration. In addition, the horizon circle is placed at

20   a zenith angle smaller than 90°, often between 85° and 79°, to eliminate the strong view distortion close to the horizon, and in some cases, objects present in the view. As explained earlier, the zenith angle resolution per pixel exceeds 1.2° close to the horizon. The information value for zenith angles larger than 80° is diminished. These pixels ~~should be~~ are excluded from the analysis. Practically, this is a very thin ring cut from the original image but does help eliminate false signals ~~from~~ at low sun angles. The current process requires to find these calibrations for a small ~~handful~~ sampling of images in a series, and to then

25   apply them to all images in the series.

Step (3) removes the perspective distortion. The projection of the sky onto the plain of an image introduces a perspective distortion, as described in Long et al (Long et al., 2006). A coordinate transformation is performed to represent the sky within the horizon circle in terms of azimuth and zenith angles. The azimuth is the same in both projections. Zenith angle θ relates to the radial distance r in the original image from the centre of the horizon circle as $r = R \sin\theta$. While R is not determined,

30   image horizon radius R_H and horizon zenith angle θ_H provide one known point to allow for proportional scaling. The

Formatted: Highlight

coordinate transformation represents the sky circle in a way in which radial distance from zenith s_z scales with zenith angular coordinate θ as

$$s_z = \frac{R_H}{\sin\theta_H} \times \theta$$

(9)

5 ~~We tested the influence of the spherical mirror reflection on the distortion. For camera positions at height h above a convex mirror of radius A where $h/A \approx 1$, the assumption $\theta \sim s_z$ is reasonable.~~ One of the visible effects of this transformation concerns 22° halos: in the original TSI image, a halo appears as a horizontal ellipse; after the transformation it will have a shape closer to a circle.

Step (4) identifies the solar position and masks non-sky details. The position of the sun is marked based on the geographical
10 position of the TSI and the Universal Time (UTC) of the image. Extraneous details, such as the shadow strip, the area outside the horizon circle, the camera, and the camera mount, are masked. The centre panel of ~~Figure 1~~Fig. 2 shows the image produced by all these adjustments up to step (4). Since often the position of the sun is detectable in the image, the marked sun position serves to refine the calibrations described above.

In step (5), the standardized local sky map (LSM) is created. A sketch of the layout of the LSM is provided in ~~Figure 2~~Fig. 3.
15 The LSM provides a standard sky section, centred at the sun, oriented with the horizon at the bottom, and presented in the same units for all possible TSI images (independent on the resolution of the original). Units of measurement in the LSM are closely related to angular degrees, but do not match perfectly due to a zenith-angle dependence of the azimuth arc length. The LSM is generated by rotating and cropping the image from step (4) to approximately within 40° of the sun, with the sun at its centre.

20 The side length of the LSM in pixels scales with the previously determined horizon radius R_H in pixels and the corresponding maximum zenith angle θ_H in ° as

$$w_{LSM}(pixels) = \frac{R_H(pixels)}{\theta_H(degrees)} \times 40°$$

(10)

Equation (10) provides a unit transformation between pixel positions and LSM units. For a TSI image of size 480×640 pixels,
25 the LSM will have a size of approximately 240×240 pixels. For the earlier, smaller TSI images, the LSM has a size of approximately 140×140 pixels. The unit scaling includes the calibration choices R_H and θ_H, hence there is a slight variation in LSM ~~pixel sizes~~ side lengths. We eliminate the influence of the varying ~~pixel~~ LSM sizes by performing all algorithm operations in standardized LSM units, which roughly correspond to angles of 1°. In other words, all LSM are equivalent to each other in terms of their LSM units, but not in terms of pixel positions. At $\theta = 45°$, the arc length of azimuth angle φ is
30 equivalent to the arc length of θ of same size; however, if $\theta > 45°$ the azimuth arc is stretched, requiring an additional horizontal compression to ensure equivalence of horizontal and vertical angular units. ~~The algorithm is robust enough to allow this scaling~~

45

Formatted: Font: Italic
Formatted: Font: Italic
Formatted: Font: Italic
Formatted: Font: Italic

~~by solar position alone, without loss of efficacy.~~ The LSM is divided into quadrants, shown in ~~Figure 2~~Fig. 3, which are analyzed and classified separately by the algorithm described in the next section.

2.3 Computing Sky Type and Halo Properties

5 **2.3.1 Average radial intensity (ARI)**

Halos, as sun-centred circles, are creating a brightness signal at a scattering angle of 22□. We found it useful to analyse the radial brightness $I(s)$ with s being the radial distance from the sun in the image plane, similar to the halo detection algorithm by Forster (Forster et al., 2017).. The term intensity refers to the colour values of any of the colour channels, and varies between

0 and 255. There is a physical reason for using $I(s)$ in cloud assessment. The presence of scattering centres in the atmosphere

10 influences the properties of sky brightness in the near-sun sky section. A very clear atmosphere, for example, exhibits an exponential decline, but with relatively high intensity values in the blue channel due to Rayleigh scattering. In case of cirrostratus, the increased forward scattering of larger particles (in this case ice crystals) leads to a decreased gradient of radial brightness, with more evenly distributed intensities in the red, green, and blue channels. In a partially cloudy sky, we would find sharp variations in $I(s)$, varying with colour channel. An overcast sky, on the other hand, may exhibit no decline in radial

15 brightness, and will generally have low intensity values across all colour channels. A sketch of the LSM is given in ~~Figure 2~~ Fig. 3. The radial intensity $I(s)$ is computed using the colour intensity values of the image (0 to 255), separated by

colour channel. The LSM is divided into four quadrants: TR = top right, BR = bottom right, BL = bottom left, TL = top left, analysed separately, and then recombined for the image scores. The division into quarters allows to accommodate partial halos, low solar positions, and the influence of low clouds in partially obstructing the view to cirrostratus. The algorithm uses various

20 properties of $I(s)$ to assign STS and IHS, as detailed below. The average radial intensity $I(s)$ is computed as an average over pixels at constant radial distance s from the sun. Due to the low resolution of the LSM, and due to some noise in the data, we average $I(s)$ over a circular ribbon with a width of 4 pixels, centred at s. Computing $I(s)$ over a thin ribbon addresses issues encountered when averaging over a circle in a coarse square grid, allowing continuity where otherwise pixilation may interrupt the line of the circle. Figure 3 Figure 4 shows the radial intensity of the red channel (R) in the bottom right quadrants of the

25 LSMs featured in Figure 1 Figure 2. Panel A includes $I(s)$, a linear fit, as well as the running average I_6, plotted versus radial distance s. The running average is taken as the average of $I(s)$ over a width of 6 LSM units centred at s:

$$\bar{I}(s) = \frac{1}{N} \sum_{s-3 \, LSMunits}^{s+3 \, LSMunits} I(s)$$

(11)

The clear-sky image exhibits a lower red intensity overall than the halo image. The halo presents as a brightness fluctuation at

30 about 21 LSM units. The resolution of the TSI images only allows to resolve 0.4□ to 0.7□ with certainty, and variations in calibration and zenith angle do influence

47

~~deviations from the expected 22 position.~~ The analysis of $I(s)$ is undertaken in

an

interval between 15 and 26 LSM units, called the radial analysis interval (RAI). The RAI is marked in ~~Figure 2~~ Fig 3. A linear fit yields a slope and intercept value used for the STS. We define the radial intensity deviation as

$$\eta(s) = I(s) - \bar{I}_6(s)$$

(12)

Panels B in ~~Figure 3~~Fig. 4 show $\eta(s)$ for both situations. The details of the halo signal in $\eta(s)$ contribute in particular to the computation of the IHS.

2.3.2 Sky type score (STS)

Properties of $I(s)$ were computed for the set of 80 seed images mentioned in ~~section 1~~Sect. 1. Twenty images for each sky type were divided further by sky quadrants, yielding between 60 and 80 property sets for each sky type to ~~seed~~ initiate the master table. Some quadrants were eliminated by horizon-near solar positions. These image quadrants were used to apprise the utility of properties in making sky type assignments, with focus on the radial analysis interval (RAI) between 15 and 26 LSM units. The ten image properties used to compute the STS are listed in Table 3~~., together with~~Also listed are their average values ~~for~~and standard deviations as computed from a later and more complete version of the master table. ~~values for the master table.~~ The ten image properties ~~They~~ include the slope and intercept of the line fit to $I(s)$ for each colour channel, where the slope characterizes a general brightness gradient, and the intercept gives access the overall brightness in the RAI. The line fit alone will not allow to differentiate partially cloudy skies from other sky types. However, the presence of sharply outlined clouds leads to a larger variation in intensity values, even for the same radial distance from the sun. The areal standard deviation (ASD) is an average of the standard deviation of $I(s)$ for each radial distance s, averaged over all radii separated by colour channel. To set apart clear skies, the average colour ratio (ACR) in the analysis area is computed as

$$ACR = \frac{B^2}{GR}$$

(13)

In ~~Figure 4~~Fig. 5, the STS property set is represented graphically, including means, standard deviations, and extreme values as observed in the master table. Clearly, no single property alone will suffice to assign sky type reliably. There is overlap in the extreme ranges. Relations between the colour channels are influential, as well. We are using the mechanism described in section 2.1, Eqns (1) through (6). The ~~continually refined~~ master table ~~defines~~ computes a mean value vector M, see Eq. (2), and inverse covariance matrix Σ^{-1}, see Eq. (4), for each sky type. The mean values for M are given in Table 3~~Table 3~~, together with their standard deviations for the training set of images. As a new image is processed, its STS property vector X, Eq. (1), is computed for each sky quadrant. Subsequently, a score is computed for each sky type using Eq. (6). The coefficient C_0 in Eq. (6) is arbitrary. In the STS computation, a~~A~~ value of ~~10^5~~10^3 was used for C_0 which places a rough separator of order 1 between images that match closely a particular sky type, and those which do not. The raw values of F in Eq.(6) vary greatly even between similar looking images, hence the STS is computed as a relative contribution between 0 and 100% for each sky type and each quadrant. For the CS score this would mean:

49

$$STS(CS) = \frac{F_{CS}}{F_{CS} + F_{PCL} + F_{CLD} + F_{CLR}} \times 100\%$$

(14) This means, a single image quadrant can carry scores of 45% for CS, 35% for PCL, and 20% for CLD. The dominant sky type then is CS for this quadrant, since it contributes the largest score. The STS for the image is assigned as the average over all

5 quadrants. If the raw scores F for all sky types were smaller than 10^{-8} the images is classified as N/A. It simply means that its properties are not close to any of the sky type categories. Such conditions may include overexposed images, horizon-near solar positions, a bird sitting on the mirror, and other conditions that produce images very different from the sky types sought after. Also classified as N/A are quadrants in which the average radial intensity lies above 253 (overexposure), or contains a large fraction of horizon (bottom quadrants in low sun positions). A one-day sample of sky type data is shown in ~~Figure 5~~Fig. 6, for

10 10 March 2018. The day was chosen for its variability, including periods of each of the sky types, as well as clearly visible halo periods. The central panel tracks STS for all sky types through the day, ~~taken for the combined sky~~ taken for all ~~4~~ four LSM quadrants combined. It is important to note that the sky type only can be representative of the section of sky near to the sun. The white areas of 25 or 50 % are introduced when the solar position nears the horizon, eliminating the two bottom quadrants of the LSM from analysis. Some of the late-day images contain quadrants that were eliminated due to overexposure.

15   The white scattering disk around the sun near the horizon does not allow for analysis, exemplified in the sample image at

50

22:53:00 UTC included in ~~Figure 5~~Fig. 6. For large portions of the day, the dominant sky types have been classified as CS and PCL, and the images corroborate this. The 14:36:00 image shows a thicker cloud cover, and the algorithm correctly responds by increasing the CLD score. At 21:00:00, the algorithm indicates an increased CLR score, consistent with the visual inspection of the TSI image at the time. Given the simplicity of this sky type assessment, we believe that this radial scattering analysis

20 around the sun has the potential to address some of the challenges that have been encountered using a simple cloud fraction in radiation modelling (Calbó and Sabburg, 2008; Ghonima et al., 2012; Kollias et al., 2007). The variation in radial intensity gradient as scatterers are present along the optical path can provide an alternative assessment for the presence of cirroform clouds, solving problems of classifying near-solar pixels using a colour ratio and/or intensity value only (Kennedy et al., 2016; N. Long et al., 2006). That will be a direction to discuss and explore in the future.

25 **2.3.3 Ice halo score (IHS)**

The 22☐ halo is a signal in the image that can be obscured by many other image features, including low clouds, partial clearings, inhomogeneous cirrostratus, regions of over-exposure, and near-horizon distortions. The appearances of 22☐ halos span a wide variety of sky conditions, ranging from almost clear skies to overcast altostratus skies, with the majority of halo phenomena appearing in cirrostratus skies. The challenge to extract the halo from such a wide variety of sky conditions is formidable.

30   While the statistical approach described in Sect. 2.1 will again form the core of the approach, the challenge shifts to defining a set of suitable properties of

51

the image. In addition to the properties used in sky type assignment, the halo scoring must seek features in $\square(s)$, {Eqn. (12), that are unique in halo images, such as a minimum followed by a maximum at halo distance from

the sun. The absolute values of $\eta(s)$ are dependent on various image conditions. Due to the variety of sky conditions, and variations in calibration and image quality, the values of maximum and minimum alone are not sufficient to reliably conclude the presence of a halo. We have found instances in which $\eta(s)$ does exhibit the halo

5 maximum, but does not dip to negative values first. However, the upslope-crest-downslope sequence is consistently present in all cases of 22° halo. The halo search ~~should be~~ is undertaken for a sequence of upslope – crest – downslope in terms of radial positions and range of slopes. All three characteristics present clearly in the derivative of the $\eta(s)$, the radial intensity deviation derivative $\eta'(s)$.

10 This derivative of the discrete series $\eta(s)$ is approximated numerically by a secant methods as

$$\eta'_i \approx \frac{\eta_{i+1} - \eta_{i-1}}{s_{i+1} - s_{i-1}}$$

15 (15)

In ~~Figure 6~~Fig. 7, both $\eta(s)$ and $\eta'(s)$ are shown for the bottom-right quadrant of the green channel of the halo image in ~~Figure 1~~Fig. 2. The sequence of radial halo markers is illustrated in ~~Figure 6~~Fig. 7. The algorithm computes $\eta'(s)$ and seeks the positive maximum and the subsequent negative minimum, plus the radial

20 position of the sign-change between them. This produces a sequence of radial locations s_{up}, s_{max}, and s_{down} which basically outline the halo bump in width and location. There are often multiple maxima of $\eta'(s)$ contained in the RAI. A halo image typically has fewer maxima than a non-halo image, but of larger amplitude. Therefore, the number of maxima as well as the upslope value η'_{up}

25 ~~and down-slope derivative~~ η'_{down} join the set of halo indicators. If multiple maxima are found, the dominant range is used. Lastly, a radial sequence should be consistent across all three colour channels. The resolution of the TSI images only allows to resolve 0.4° to 1.2° with certainty; in addition variations in calibration and zenith angle do influence deviations from the expected 22°

30 position. The separation of colours observed in a 22° halo display is not resolved

53

with statistical significance, therefore this was not used as a criterion for halo detection. The, which is why a standard deviation of all three radial positions across the three colour channels was added to the halo scoring set of properties. We arrive at a set of 31 properties for the computation of the IHS, listed in Table 4, together with their means and standard deviations. ~~The means and standard deviations have been computed~~

35 ~~for the master~~ table. ~~The separation of colours observed in a 22° halo display is not resolved with statistical significance in the TSI images,~~ ~~therefore this was not used as a criterion for halo detection.~~ The mean value vector M and the inverse covariance matrix Σ^{-1} are computed in the master table and then imported by the halo searching algorithm for use in ~~equation~~ Eq. (6). The coefficient C_0 in Eq. (6) is arbitrary. In the IHS computation, a value of 10^6 was chosen for C_0 which places a rough separator of order one between image

40 quadrants that do have a halo, and those which do not. While the individual scoring works very well for halo images, it does trigger the occasional halo score for images that do not exhibit a halo. This may occur due to inhomogeneities in a broken cloud cover, or other isolated circumstances. These false halo scores often occur on isolated images. We utilize the factor of residence time of a halo to address this. In a 30-s binned series of TSI images, the halo will

appear usually in a sequence of subsequent images, often in the order of minutes or even hours. We added a Gaussian broadening to the time series of halo scores F_i, taken at times t_i with a broadening w

$$IHS(t) = \sum_{t_i=t-3w}^{t_i=t+3w} F(t_i) \exp\left[-\frac{(t_i-t)^2}{2w^2}\right]$$

(16)

5 This de-emphasizes isolated instances, and enforces sequences of halo scores, even if they exhibit weak signals or gaps. This procedure reduced the false halo identifications significantly. Just as for the sky type, the Master table is being complemented as more images are analysed. The raw halo score F is computed for the four quadrants of an individual image, their ~~sum~~ average is used to assign the raw score for the whole image. ~~In Figure 5, the time series of the IHS is shown in the bottom panel. Just as for the sky type, the Master table for sky type scores and halo scores is being complemented as more images are~~

10 ~~analysed.~~ The broadening ~~w~~ in ~~Eqn~~Eq. (16) was chosen as $w=$4 images for ~~this example, which means the~~ the IHS in Figure 6. The Gaussian half width corresponds thus to 2 minutes. ~~The broadening w in Eqn (16) was chosen as 4 images for this example, which means the Gaussian half width corresponds to 2 minutes.~~ The clear 22° halo between 19:00 and 20:00 UTC produces a strong IHS. There are a few weaker signals, and upon inspection of the images we find that these correspond to partial halos (like at 17:07:00), or halos in a more variable sky.

15 ## 3   Results for January through April 2018

We chose the record of the month of March of 2018 at the SGP location for a thorough comparison of algorithm results to visual image inspection. The complete month TSI record, starting at 1 March 2018 0:00:00 UTC ~~3/1/2018 0:00:00 UTC~~ and ending at 31 March 2018 23:59:30 UTC~~3/31/2018 23:59:30 UTC~~, contains 44,026 images. An image IHS and STS are assigned as the average over all scoring quadrants. Visual image classification for so many images poses a considerable challenge,

20 which we approached in form of an iteration. For each of the 31 days of March, an observer assigned sky classifications to segments of the day by inspecting the day series as an animation. This can easily be done by using an image viewer and continuously scrolling through the series. Then, the day would be subjected to the algorithm. The sections of the record in which visual and algorithm differed were inspected again, at which point either the visual assessment was adjusted, or the misclassified images were included in the Master table in order to train the algorithm toward better recognition. Adjustment

25 to visual classifications often occurred at the fringes of a transition. For example, when a sky transitions from cirrostratus to altostratus to stratus, the transitions are not sharp. The observer sets an image as the point in which the sky moved from CS to CLD, but the criteria in the algorithm would still indicate CS. This can affect up to a hundred images at transition times, which then were reclassified. On the other hand, if a clearly visible halo was missed by the algorithm, this would be a case for adding new property lines to the Master table in order to capture the particular conditions. After each change in the Master table, the

algorithm would be repeated, and recalibrations to the visual record, as well as to the Master table itself were made. The process was repeated several times until no more gains in accuracy were observed. These adjustments were done by SB. The resulting time lines for STS and IHS for the month of March are plotted in ~~Figure 7.~~Fig. 8. Many of the images exhibit strong indicators for multiple sky types. The largest STS is used to assign a sky type to an image. The IHS was computed using ~~a pre-factor C of 10⁶ (Eqn.6) and~~ a half width broadening in time of w=3.5 minutes (Eq~~n~~.16). ~~It is interesting to observe that~~ As expected, the high halo scores coincide with strong CS signals. Noteworthy is also, that there are a number of days in which CS does not carry a 22□ halo. Upon inspection of the numerical values for IHS, it becomes clear that `a cut-off is needed to assign an image with a label of halo/no halo in the post-processing. This cut-off value is arbitrary and dependent on factors such as w and C_0, as well as the quality of the calibration. Our testing, minimizing false negatives and maximizing correct positives, places it at around 4000 for the month of March.

In Table 5, visual and algorithm results of the sky type assignments are cross-listed. It is worth reminding the reader that sky types are assigned only for the radial analysis interval indicated in ~~Figure 2~~Fig. 3. Table 5 uses the denominations *%alg* and *%vis* to distinguish two possible reference cases. For CS, 88*%vis* means that of all visual CS skies, the algorithm correctly identifies 88 % of cases. The number 86*%alg* means that 86% of the images classified as CS by the algorithm also have been visually classified as CS. Cloudy skies are reliably identified by the algorithm. A small percentage (3%) of visual CLD skies trigger a PCL signal, mostly due to inhomogeneities in cloud cover. The algorithm classifies 95% of all visual CLR skies correctly. Differentiating between CS and PCL is very successful~~.,~~. ~~but~~However, ~~each of these~~these two sky types ~~exhibit~~ pose some difficulties. For example, 8.5% if visual CS skies scored a CLR signal, and 10% of images classified as CS were visually assigned a PCL sky type. In these cases we often found that

56

the algorithm assignment might be more persuasive than the visual assignment –
30 a visual assignment is a subjective call, and open to interpretation of the
observer. Combined with image distortion and resolution limits, it is quite
possible that the visual assignments carry a considerable uncertainty. Some of the
visual CS skies, for example, present to the eye as CLR, but reveal the movement
of a cirrostratus layer if viewed in context of time-development (animation).
35 Similarly, cirrostratus may present as an inhomogeneous layer in transition skies,
triggering a ~~partly-cloudy~~PCL assessment in the algorithm. Low solar positions are
prone to larger image distortion, which may lead to misinterpretation. It is ~~also~~
worth noting that every image quadrant receives an STS for all sky types from the
algorithm~~, and~~ ~~that the total image assessment merely selects for the STS with~~
40 ~~the highest contribution~~. In cases of mismatch, we often find that the two sky
types at conflict both contribute significantly to the STS of the image. If the solar
zenith angle is above 68□, no sky type assignments were made. Most of the 397
CLR images that presented as CS to the algorithm were taken at very low sun,
with a significant over-exposure disk in near-solar position. Table 5 also lists a
45 comparison of visual halo identifications with the algorithm scores. According to
this assessment, the algorithm correctly calls 85 % of visual halo images, while
not diagnosing 15 % of them. On the other hand, 12 % of all halo signals do not
correspond to a halo in the image. One can improve the correct identification rate
by lowering the cut-off score, on the cost of an increase in the signal from false
50 identifications. Balancing the false positive and false negatives yields a reliability
of about 12 to 14 %. Some of the false negatives arise from altocumulus skies, in
which the outlines of cloudlets may trigger halo signals by their distribution and
size. These are very difficult to discriminate from visual halo images. Some images
were flagged with an IHS by the algorithm, and the presence of a weak halo
55 revealed itself only after secondary and tertiary inspection of the image.
Caution~~Some caution~~ is advised in relying heavily on visual classifications of TSI

57

images alone. The visual sky type and halo assignments themselves have an uncertainty due to subjectivity. While it is easy to distinguish a partially cloudy sky from a clear sky, this may become difficult for the difference between thick cirrostratus and stratus. Their visual appearances may be quite similar. Sometimes, an assignment can be made in context of temporal changes. Some clear-appearing skies reveal a thin cirrostratus presence if viewed in a time series instead of in an individual image. We also have found visual halos in images which this algorithm flagged, and the presence of a weak halo revealed itself only after secondary and tertiary inspection of the image. It is therefore a future necessity to combine the visual assignments of sky types with LIDAR data for altitude, optical thickness, and depolarization measurements to make an accurate assessment of the efficacy of the halo detection sky type identification, following closely the processes described by Sassen et al. (Sassen et al., 2003) and Forster et al. (Forster et al., 2017).

We applied the algorithm to the TSI record for the first four months of 2018 for the SGP ARM site. It is worth noting that this paper is not intended to present a complete exploration of the ARM record concerning 22☐ halos. We are, however, including a demonstration of capacity of the algorithm presented here. Table 6 summarizes our findings. It lists the percentages for the four sky types by month. A portion of the images has not been assigned with an STS. The conditions under which this occurs have been alluded to earlier, and include horizon-near solar positions, images with over exposure in the RAI, and images for which the raw STS for each sky type was numerically too low to be considered a reliable assessment. Therefore, sky type percentages refer only to all identified images. January and March exhibited a large fraction of clear skies. February was dominated by cloudy skies, while April registered a high percentage of CS - however, only a partial month of images was available for April. Sky type depends strongly on the synoptic situation. That means that no further

58

85   conclusions should be made from these data. The 22◻ halo statistics in Table 6 lists data on the 22◻ halo, including duration, number of incidents, and data on partial halos. The partial halo data are based on the individual quadrant IHS for an image, while the image score is used for duration and incidence information. The number of separate halo incidences counts sequences of images for which the

90   IHS did not fall below the cut-off value of 4000. While it is worth noting that the number of incidences lies in the order of magnitude of the number of days in a month, it is certain that the halo instances are not evenly distributed. ~~Figure 7~~ Figure 8 does demonstrate this behaviour. However, even on a day of persistent cirrostratus with 22◻ halo, interruptions of its visibility can occur. Sometimes low

95   stratocumulus may obscure the view of the halo, sometimes the cirrus layer is not homogeneous. This may lead to a large number of separate halo incidences in a short time, while none are counted at other times. The mean duration of a halo incident lies between 16 and 34 minutes, depending on month. We listed the maximum duration found in each month as well. The longest halo display in the

100   time period occurred in April 2018, with nearly 3.5 hours. Mean values are easily skewed by a few long-lasting displays. ~~Figure 8~~Figure 9 shows the distribution of 22◻ halo durations for the four months. The most common duration of a 22◻ halo lies between 5 and 10 minutes, followed by 10 to 15 minutes. Due to the time-broadening applied via Eq.~~n~~ (16), the display time cannot be resolved below

105   3 minutes. We consider the fraction of images in which a halo was registering. That marker varied between 3.9% for January and 9.4% for April. In accord with findings in (Sassen et al., 2003), we find a low amount of halo display activity in January. However, this may be influenced by the large zenith angles for the sun in January. The closer the sun to the horizon, the more TSI images have been

110   excluded from the analysis, and the stronger the influence of distortion ~~— both effects that would influence both studies~~.

Occasionally, only partial halos will be seen, depending on positioning of the cirroform clouds and on obstruction by low clouds. The division of the LSM into quadrants allows to assess the possibility of fractional halos, as indicated in

115 Table 6. The overwhelming portion of halo incidences shows full or 75% halo. This means that in four or three of the quadrants, the IHS has exceeded its minimum cutoff. Quarter halos have only rarely registered in the algorithm. Many of the half halos can be found for images taken close to sunrise or sunset. That explains their relative frequency in January and February.

120 We started the project with the goal to find information on cirrostratus composition, in particular with respect to assessments of variation of smooth versus rough crystals. Forster et al (Forster et al., 2017) discuss that the necessary fraction of smooth crystals for a halo appearance lies between 10% and 40%. The authors observe a 22☐ halo for 25% of all cirrus clouds for a 2.5-

125 year photographic record taken in Munich, Germany. The bottom part of Table 6 investigates the relation between sky type and 22☐ halo incidences. The first set of data in the Relations section of Table 6 gives the fraction of each sky type, as it produced a~n 22☐ halo incident. For example, in January we found that 9 % of all cirrostratus skies were accompanied by a 22☐ halo. In the data for April, this

130 fraction increased to 22% of all cirrostratus skies. We also have registered halos for a portion of partly cloudy skies, and for cloudy skies. No halos have been registered in any of the clear skies. This is certainly consistent with the observations of Forster et al (Forster et al., 2017). However, we must consider reasons for the PCL and CLD halo incidences. Upon random sampling of these

135 combinations we find the following: The PCL indicator has been assigned to images that have a highly varied cirroform sky, including halo appearances. In a few instances, low clouds triggered the PCL indicator, however, a CS layer at higher altitude still contributed a halo score above the threshold. Many of the halo scores in CLD skies belong to images with a cloudyan overcast appearance,

Formatted: Highlight

140   however, most likely belong to a thickening and lowering altostratus as often found in warm front approaches. ~~So, these~~These are not false signals, but certainly conditioned by the limitations of the sky type classification. The second set of numbers in Table 6~~Table 6~~ shows the fraction of all halos associated with the various sky types. In January, 49% of all halo incidences occurred in CS skies,

145   while in March this number was 87%. ~~One of the conclusion to be made from the relation between STS and IHS concerns the confidence in the presence of smooth crystalline habits among the cloud particles, as shown only in a one-fifth fraction of all cirrostratus. If the halo algorithm is~~ With the halo algorithm used on TSI images to identify the appearance of 22□ halos, the next useful and logical step

150   will be to relate these data to other instrument records: LIDAR for altitude, particle density, and particle phase (solid or liquid), photometric measurements to glean information on radiative flux. ARM sites have accumulated such instrumental data. The algorithm proposed here will make such data investigation possible, and delivers support for crystal identification.

Finally, it is worth discussing the general approach of the TSI algorithm in comparison to the halo detection algorithm developed by Forster et al (Forster et al., 2017). Both algorithms utilize features found in the radial intensity $I(s)$, such as the sequence of minimum – maximum at the expected radial positions in order to find halos in an image. The random forest classifier approach described in (Forster et al., 2017) is a machine learning approach that arrives at a binary conclusion for an

5 image in form of halo/no halo. Their algorithm was trained on a visually classified set of images in order to construct a suitable decision tree. In addition to 22□halos, the Forster algorithm also identifies parhelia and other halo display features in images taken by a high-resolution, sun-tracking halo camera. The algorithm presented here for TSI data must work with a much less specialized set of images, notably of lower resolution. It does not characterize halos in a binary decision, but rather assigns a continuous ice halo score to an image, in addition to sky type scores for four different types of sky conditions. Similar to the

10 Forster algorithm, the TSI algorithm also was trained on a visually classified set of images. ~~F~~For the algorithm presented here, ~~f~~further training is easy to incorporate via a master table ~~which provides means and covariance matrices to the algorithm~~. Both algorithm have overlap. The TSI algorithm makes extensive use of the radial brightness gradient (slope) for the sky type assignments. The relation of this gradient to the physical presence of scatterers along the optical path makes this an attractive approach.

15 4 Summary

ARM sites have produced long-term records of sky images. We developed an algorithm that assigns sky type and halo scores to long-term series of TSI images with the goal of using these long-term image records to provide supporting information the presence of smooth, hexagonal ice crystals in cirrus clouds from

observations of 22□ halos ~~, we developed an algorithm that~~ ~~assigns sky type and~~ ~~halo scores to long-term series of TSI images..~~ ~~With the goal of using these long-~~ ~~term image records to~~

20 ~~provide supporting information the presence of smooth, hexagonal ice crystals in~~ ~~cirrus clouds from observations of 22□ halos , we developed an algorithm that~~ ~~assigns sky type and halo scores to long-term series of TSI images.~~ We described this algorithm in this paper, including the image preparation to generate a standardized image section centred at the sun, called the Local Sky Map (LSM). A multivariate analysis of selected LSM properties, as supported by a master table, allows the assignment of scores with respect to sky type and 22□ halo presence in the solar-near section of the sky. In particular, we focus

25 on the properties associated with the radial brightness behaviour around the sun. Physically, the number and type of scattering centres in the atmosphere does influence the brightness gradient, thus giving us access to an assessment of cloud type and cloud cover. The brightness fluctuation associated with the 22□ halo provides a further set of properties specific to the presence of a 22□ halo. We analyse all four quadrants adjacent to the sun separately, then combine the scores into a raw image score. For the ice halo score, we also apply a Gaussian broadening across the time series. The algorithm has been found to be about

30 90% in agreement with the visually assigned sky type, and 85% in agreement with the visually identified ice halo score. The application to the first four months of the TSI records from SGP ARM site indicates periods of halo displays, with a most common duration of about 5 to 10 minutes, but lasting up to 3 hours. It allowed to identify the fraction of cirrostratus skies

that do produce halo displays, as well as find such data for other sky types as well. In the future, the algorithm will be applied to deliver 22° halo data for the long-term TSI records accumulated in various geographical locations of ARM sites, and allows further investigation into correlations with other instrumental records from those sites.

5 In particular, LIDAR data for altitude and optical thickness measurements, as well as depolarization analysis will be a useful combination with this photographic halo display record. It is reasonable to expect that the reference set for sky type determination will improve with the support of LIDAR data. The method described here may be suitable to expand to other types of sky analysis on TSI

10 images.

Author contribution

Sylke Boyd is the main author of this paper and the code. The four co-authors worked on the algorithm as undergraduate researchers. Stephen Sorenson decided on the use of C++ and opencv3.2 for image manipulation, and initiated

15 the program code. Shelby Richard worked out the details of the radial intensity computation and properties. Michelle King and Morton Greenslit contributed algorithm parts to eliminate optical distortions and low-cloud obstruction, and input management. SR, MK, and MG all contributed to data collection and analysis.

20 **Acknowledgement**

30   **Competing Interests**

The authors declare that they have no conflict of interest.

Code availability

Code and accessory files are made available at github under DOI 10.5281/zenodo.8475 (Boyd et al., 2018).

35

References

Bailey, M. P. and Hallett, J.: A Comprehensive Habit Diagram for Atmospheric Ice Crystals: Confirmation from the Laboratory, AIRS II, and Other Field Studies, Journal of the Atmospheric Sciences, 66, 2888-2899, 2009.

Baran, A.: A review of the light scattering properties of cirrus, 2009.

5   Boyd, S., Sorenson, S., Richard, S., King, M., and Greenslit, M.: Haloloop software. https://zenodo.org/badge/latestdoi/157256231, 2018.
Calbó, J. and Sabburg, J.: Feature Extraction from Whole-Sky Ground-Based Images for Cloud-Type Recognition, Journal of Atmospheric & Oceanic Technology, 25, 3-14, 2008.
Campbell, J. R., Lolli, S., Lewis, J. R., Gu, Y., and Welton, E. J.: Daytime Cirrus Cloud Top-of-the-Atmosphere Radiative Forcing Properties at a Midlatitude Site and Their Global Consequences, Journal of Applied Meteorology & Climatology, 55, 1667-1679, 2016.

10   Cziczo, D. J. and Froyd, K. D.: Sampling the composition of cirrus ice residuals, Atmospheric Research, 142, 15-31, 2014.

ENA, A.-T. a.: 2013, updated hourly. Total Sky Imager (TSISKYIMAGE). 2013-10-01 to 2018-05-28, Eastern North Atlantic (ENA) Graciosa Island, Azores, Portugal (C1). Compiled by V. Morris. Atmospheric Radiation Measurement (ARM) Climate Research Facility Data Archive: Oak Ridge, Tennessee, USA. Data set accessed 2018-06-07 at http://dx.doi.org/10.5439/1025309., 2018.

Fasullo, J. T. and Balmaseda, M. A.: Earth's Energy Imbalance, Journal of Climate, 27, 16p, 2014.

15   Fasullo, J. T. and Kiehl, J.: Earth's Global Energy Budget, Bulletin of the American Meteorological Society, 90, 13p, 2009.

Fasullo, J. T., von Schuckmann, K., and Cheng, L.: Insights into Earth's Energy Imbalance from Multiple Sources, Journal of Climate, 29,

11p, 2016.

Forster, L., Seefeldner, M., Wiegner, M., and Mayer, B.: Ice crystal characterization in cirrus clouds: a sun-tracking camera system and automated detection algorithm for halo displays, Atmos. Meas. Tech., 10, 2499-2516, 2017.

20   Fu, Q., Lohmann, U., Mace, G. G., Sassen, K., and Comstock, J. M.: High-Cloud Horizontal Inhomogeneity and Solar Albedo Bias, Journal of Climate, 15, 19p, 2002.

Ghonima, M. S., Urquhart, B., Chow, C. W., Shields, J. E., Cazorla, A., and Kleissl, J.: A method for cloud detection and opacity classification based on ground based sky imagery, Atmospheric Measurement Techniques, 5, 2881-2892, 2012.

Greenler, R.: Rainbows, Halos, and Glories, Cambridge University Press, Cambridge, 1980.

25 Hammer, A., Monahan, A. H., Schmidt, T., and Heinemann, D.: Simulating clear-sky index increment correlations under mixed sky conditions using a fractal cloud model, Solar Energy, 150, 10p, 2017.

Hammer, E., Bukowiecki, N., Luo, B. P., Lohmann, U., Marcolli, C., Weingartner, E., Baltensperger, U., and Hoyle, C. R.: Sensitivity estimations for cloud droplet formation in the vicinity of the high-alpine research station Jungfraujoch (3580 m a.s.l.), Atmos. Chem. Phys., 15, 10309-10323, 2015.

30   Heymsfield, A. J., Schmitt, C., and Bansemer, A.: Ice Cloud Particle Size Distributions and Pressure-Dependent Terminal Velocities from

In Situ Observations at Temperatures from 0° to −86°C, Journal of the Atmospheric Sciences, 70, 4123-4154, 2013.

Hong, Y., Liu, G., and Li, J.-L. F.: Assessing the Radiative Effects of Global Ice Clouds Based on CloudSat and CALIPSO Measurements, Journal of Climate, 29, 7651-7674, 2016.

Ilie, A. and Welch, G.: Ensuring color consistency across multiple cameras, 17-21 Oct. 2005 2005, 1268-1275 Vol. 1262.

35 IPCC: Climate Change 2013: The Physical Science Basis. Contribution of Working Group I to the Fifth Assessment Report of the Intergovernmental Panel on Climate Change, Cambridge, United Kingdom and New York, USA, 1535 pp., 2013.

IPCC: Climate Change 2014: Synthesis Report. Contribution of Working Groups I, II and III to the Fifth Assessment Report of the Intergovernmental Panel on Climate Change Geneva. Switzerland, 151 pp., 2014.

Kandel, R. and Viollier, M.: Observation of the Earth's radiation budget from space, Observation du bilan radiatif de la Terre depuis l'espace, 40 342, 286-300, 2010.

Kennedy, A., Dong, X., and Xi, B.: Cloud fraction at the ARM SGP site: reducing uncertainty with self-organizing maps, Theoretical & Applied Climatology, 124, 43-54, 2016.

Kollias, P., Tselioudis, G., and Albrecht, B. A.: Cloud climatology at the Southern Great Plains and the layer structure, drizzle, and atmospheric modes of continental stratus, Journal of Geophysical Research: Atmospheres, 112, 2007.

45 Long, C. N., Sabburg, J. M., Calbó, J., and Pagès, D.: Retrieving Cloud Characteristics from Ground-Based Daytime Color All-Sky Images, Journal of Atmospheric and Oceanic Technology, 23, 633-652, 2006.

N. Long, C., M. Sabburg, J., Calbó, J., and Pages, D.: Retrieving Cloud Characteristics from Ground-Based Daytime Color All-Sky Images, 2006.

NSA, A.-T. a.: Atmospheric Radiation Measurement (ARM) Climate Research Facility. 2006, updated hourly. Total Sky Imager 50 (TSISKYIMAGE). 2006-04-25 to 2018-04-11, North Slope Alaska (NSA) Central Facility, Barrow AK (C1). Compiled by V. Morris. Atmospheric Radiation Measurement (ARM) Climate Research Facility Data Archive: Oak Ridge, Tennessee, USA. Data set accessed 201806-07 at http://dx.doi.org/10.5439/1025309., 2018.

OLI, A.-T. a.: Atmospheric Radiation Measurement (ARM) Climate Research Facility. 2013, updated hourly. Total Sky Imager (TSISKYIMAGE). 2013-08-30 to 2018-05-24, ARM Mobile Facility (OLI) Olikiok Point, Alaska; AMF3 (M1). Compiled by V. Morris.

Atmospheric Radiation Measurement (ARM) Climate Research Facility Data Archive: Oak Ridge, Tennessee, USA. Data set accessed 201806-07 at http://dx.doi.org/10.5439/1025309., 2018.

Sassen, K.: Corona-producing cirrus cloud properties derived from polarization lidar and photographic analyses, Appl. Opt., 30, 3421-3428, 1991.

5 Sassen, K., Zhu, J., and Benson, S.: Midlatitude cirrus cloud climatology from the Facility for Atmospheric Remote Sensing. IV. Optical displays, Appl. Opt., 42, 332-341, 2003.

Schwartz, S. E., Charlson, R. J., Kahn, R., and Rodhe, H.: Earth's Climate Sensitivity: Apparent Inconsistencies in Recent Assessments, Earth's Future, 2, 601-605, 2014.

SGP, A.-T. a.: Atmospheric Radiation Measurement (ARM) Climate Research Facility. 2000, updated hourly. Total Sky Imager [10] (TSISKYIMAGE). 2000-07-02 to 2018-04-19, Southern Great Plains (SGP) Central Facility, Lamont, OK (C1). Compiled by V. Morris. Atmospheric Radiation Measurement (ARM) Climate Research Facility Data Archive: Oak Ridge, Tennessee, USA. Data set accessed 201806-07 at http://dx.doi.org/10.5439/1025309., 2018.

Tape, W. and Moilanen, J.: Atmospheric Halos and the Search for Angle X, American Geophysical Union, 2006.

Tian, L., Heymsfield, G. M., Li, L., Heymsfield, A. J., Bansemer, A., Twohy, C. H., and Srivastava, R. C.: A Study of Cirrus Ice Particle [15] Size Distribution Using TC4 Observations, Journal of the Atmospheric Sciences, 67, 195-216, 2010.

Trenberth, K. E., Zhang, Y., and Fasullo, J. T.: Relationships among top-of-atmosphere radiation and atmospheric state variables in observations and CESM, Journal of Geophysical Research: Atmospheres, 120, 10,074-010,090, 2015.

Um, J. and McFarquhar, G.: Formation of atmospheric halos and applicability of geometric optics for calculating single-scattering properties of hexagonal ice crystals: Impacts of aspect ratio and ice crystal size, 2015.

[20] van Diedenhoven, B.: The effect of roughness model on scattering properties of ice crystals, Journal of Quantitative Spectroscopy & Radiative Transfer, 178, 8p, 2016. van Diedenhoven, B.: The prevalence of the 22 deg halo in cirrus clouds, Journal of Quantitative Spectroscopy & Radiative Transfer, 146, 5p, 2014. van Diedenhoven, B., Marshak, A., Dunagan, S., Holben, B., and Slutsker, I.: Cloud thermodynamic phase detection with polarimetrically [25] sensitive passive sky radiometers, Atmospheric Measurement Techniques, 8, 18p, 2015.

Waliser, D. E., Li, J.-L. F., Woods, C. P., Austin, R. T., Bacmeister, J., Chern, J., Del Genio, A., Jiang, J. H., Kuang, Z., Meng, H., Minnis, P., Platnick, S., Rossow, W. B., Stephens, G. L., Sun-Mack, S., Tao, W.-K., Tompkins, A. M., Vane, D. G., Walker, C., and Wu, D.: Cloud ice: A climate model challenge with signs and expectations of progress, Journal of Geophysical Research: Atmospheres, 114, 2009.

Yang, P., Liou, K.-N., Bi, L., Liu, C., Yi, B., and Baum, B. A.: On the radiative properties of ice clouds: Light scattering, remote sensing, [30] and radiation parameterization, Advances in Atmospheric Sciences, 32, 32-63, 2015.

Table 1. TSI data set properties. Seed images for the algorithm were taken from all three locations.

Location	Dates and times (UTC)		Image interval	Resolution (pixels)
Southern Great Plains (SGP, 2018) 36° 36' 18" N, 97° 29' 6" W	2 Jul 2000 0:35:00 15 Aug 2011 22:17:30	15 Aug 2011 01:17:30 19 Apr 2018 01:02:00	30 s 30 s	288☐352 480☐640
North Slope of Alaska (NSA, 2018) 71° 19' 22.8" N, 156° 36' 32.4" W	25 Apr 2006 21:44:00 9 Mar 2011 01:08:30	2 Nov 2010 21:31:00 11 Apr 2018 18:59:30	30 s 30 s	288☐352 480☐640
Eastern North Atlantic (ENA, 2018) 39° 5' 29.76" N, 28° 1' 32.52" W	1 Oct 2013 08:13:00	28 May 2018 21:04:00	30 s	480☐640

21

Table 2 Sky Type descriptions
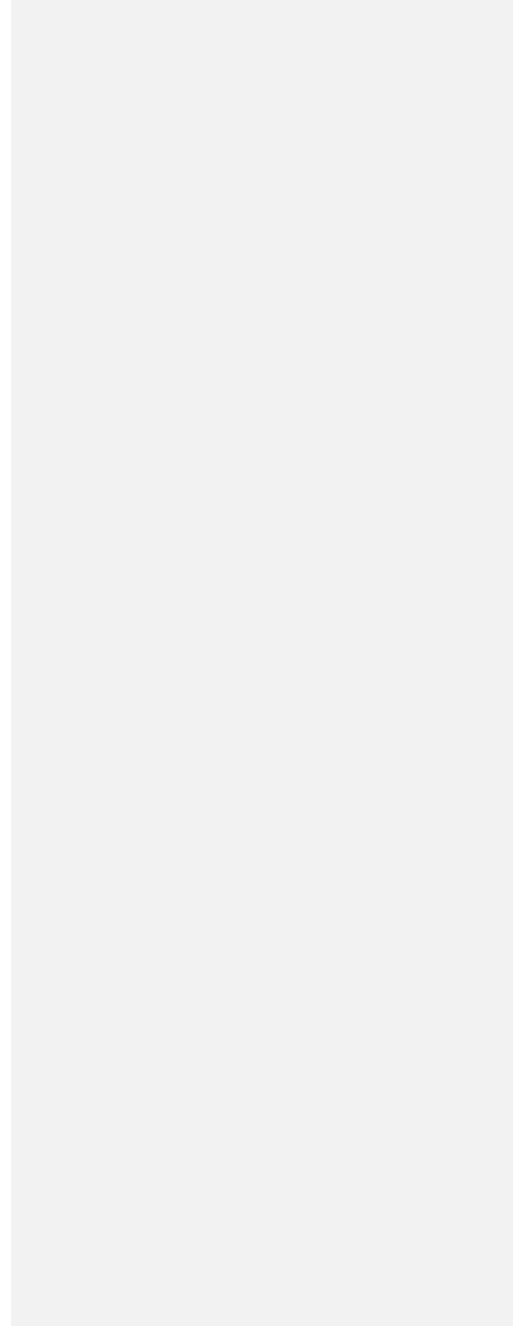
Sky type		Visual description
Cirrostratus	CS	Muted blue, no sharp cloud outlines; solar position clearly visible, bright scattering disk or halo may be present; changes are gradual and slow (several minutes)
Partly cloudy	PCL	Variable sky with sharply outlined stratocumulus or altocumulus; variations between sky quadrants; sun may be obscured; changes are abrupt and fast (less than two minutes)
Cloudy	CLD	Sun is obscured; low brightness; low blue intensity values; stratus, nimbostratus, altostratus, or cumulonimbus; changes occur slowly (order of hours)
Clear	CLR	Blue, cloud-free sky; sun clearly visible and no bright scattering disk around it; changes are slow (order of hours)
No data	N/A	This may occur at low sun positions for the bottom quadrants of the LSM, or due to overexposure in the near-solar region of the image; it's the default at night.

Table 3 STS properties, their averages, and standard deviations for ~~the~~ each sky type in the Master table. All units based on colour intensity values and LSM units. The sky type assignment is based on visual assessment the images. Number of records for each sky type is indicated in parentheses.

STs property	CS (155)	PCL (99)	CLD (93)	CLR (96)
Slope a	B -3.0 □1.5	B -1.6 □2.2	B -0.7 □1.7	B -2.3 □1.6
	G -3.2 □1.7	G -1.6 □2.2	G -0.7 □1.7	G -2.8 □1.6
	R -3.6 □1.9	R -1.9 □2.6	R -0.8 □1.8	R -2.8 □1.7
Intercept b	B 276 □34	B 248 □46	B 193 □40	B 248 □43
	G 271 □33	G 240 □53	G 195 □44	G 233 □47
	R 255 □48	R 228 □65	R 179 □47	R 184 □47
ASD_1	B 13.1 □5.3	B 20.5 □7.0	B 14.2 □5.0	B 15.4 □5.2
	G 15.0 □6.0	G 22.9 □7.7	G 15.0 □5.1	G 16.3 □5.3
	R 16.6 □6.6	R 25.5 □8.1	R 15.8 □5.6	R 14.8 □5.7
ACR^2	1.33 □0.36	1.24 □0.32	1.08 □0.12	2.07 □0.11

[1] Areal Standard Deviation; [2] Average Colour Ratio

5

23

Table 4 Halo scoring properties. These 31 properties define the space in which an image is scored for a halo. The averages given are from the master file and include 188 records from halo-containing sky quadrants, visually assessed.

IHS property	B	G	R
Slope a	-3.3 □1.5	-3.3 □1.6	-3.8 □1.8
Intercept b	279 □35	278 □37	268 □45
ASD	12.6 □4.7	14.8 □6.0	16.2 □6.4
Maximum upslope $\square'_{up}$	2.1 □1.3	2.1 □1.4	2.5 □1.6
Maximum downslope $\square'_{down}$	-1.6 □1.0	-1.6 □1.0	-1.8 □1.1
Upslope location s_{up}	17.5 □1.9	17.8 □2.3	17.5 □2.1
Maximum location s_{max}	18.9 □1.9	19.1 □2.3	18.8 □2.1
Downslope location s_{down}	20.0 □2.1	20.2 □2.4	19.9 □2.2
Number of maxima n_{max}	2.4	2.6	2.5
BGR consistency	$\sigma_{BGR}(s_{up}) = 0.8$	$\sigma_{BGR}(s_{max}) = 0.8$	$\sigma_{BGR}(s_{down}) = 0.9$
ACR		1.2□0.3	

5

Table 5. STS and IHS test results for SGP March 2018. Visual assignments were made iteratively in step with the algorithm results as described in section 3. Given are the percentages of images of visual type that have been assigned an algorithm type (%vis), and the percentages of the algorithm type that correspond to a visual type (%alg). For example, 88% of all visual CS skies are also classified as CS by the algorithm, but only 86% of all algorithm CS skies also identify as CS if inspected visually. Agreement combinations in bold. IHS > 4000 to count an algorithm halo.

	STS	Visual assignment											
		CS			PCL			CLD			CLR		
		N	%vis	%alg	N	%vis	%alg	N	%vis	%alg	N	%vis	%alg
Algorithm	CS	**6675**	**88**	**86**	683	11	9	38	1	0	397	4	5
	PCL	182	2	3	**5513**	**87**	**91**	176	3	3	191	2	3
	CLD	61	1	1	47	1	1	1	1	**98**	0	0	0
	CLR	641	8	6	136	2	1	6129	97	0	**10529**	**95**	**93**
	N/A	12597 (40% of all images)											

IHS	22° halo			No 22° halo		
	N	%vis	%alg	N	%vis	%alg
22° halo	**1996**	**85**	**88**	272	1	12
No 22° halo	349	15	1	**41409**	**99**	**99**

25

5

10

total number
of images
Number with
valid STS begin
date of record

Table 6. Sky type assignments and 22° halo formations during the months of January through April 2018, SGP. Percentages are with respect to all classifiable images. Times are TUC.

		Jan 2018	Feb 2018	Mar 2018	Apr 2018[1]
		36632	36011	44057	27741
		21238	23604	31398	20436
		1 Jan 2018 13:47:00 31 Jan 2018 23:50:00	1 Feb 2018 13:36:00 28 Feb 2018 23:59:30	1 Mar 2018 0:00:00 31 Mar 2018 23:59:30	1 Apr 2018 0:00:00 19 Apr 2018 1:02:00
Sky types	CS	20 %	18 %	25 %	34 %
	PCL	24 %	24 %	19 %	19 %
	CLD	11 %	33 %	20 %	25 %
	CLR	45 %	25 %	36 %	22 %
22° halos	Number of separate halo incidents	26	45	34	46
	Mean duration	16 min	22 min	34 min	21 min
	Maximum duration	62 min	136 min	171 min	208 min
	Total halo time	411 min	998 min	1160 min	963 min
	% halo instances with				
	4/4 22° halo	29 %	42 %	77 %	42 %
	¾ 22° halo	38 %	31 %	13 %	40 %
	½ 22° halo	32 %	25 %	10 %	18 %
	¼ 22° halo	1 %	1 %	0 %	0 %
Relations	% halo instances of all sky type instances				
	CS	9 %	16 %	18 %	22 %
	PCL	6 %	7 %	6 %	9 %
	CLD	4 %	5 %	10 %	12 %
	CLR	0 %	0 %	0 %	0 %
	All STS	3.9 %	8.5 %	7.4 %	9.4 %
	% sky type of all halo instances				
	CS	49 %	60 %	87 %	78 %
	PCL	42%	33 %	9 %	14 %
	CLD	2 %	5 %	3 %	5%
	CLR	0 %	0 %	0 %	0 %
	N/A	7 %	2 %	1 %	3 %

end date of record

79

[1]incomplete month

Impor

| List of images | Calibration | M $\square^{-1}$ from Master |

For each

Calibrate image for colour, orientation, and ~~Section~~Sec. 2., steps 2, 3

Identify sun position from geographical ~~Section~~Sec. 2., 4

Reposition and crop to generate sun-centered local sky map (~~Section~~Sect. 2.2, step 5)

Compute and analyze radial $I(r)$ for each image ~~Section~~Sec. 2.3.1

Compute the Is for each quadrant (as listed in Tables 3

| Compute STS for each sky
(CS, PCL, CLR, OLD)
(~~Section~~Sec 2.3.2 | Compute IHS by
(~~Section~~Sect. 2.3.3)
Running time average IHS by
quadrant Eq. (16 |

Compute image STS for each sky type and IHS as averages over all

Sav STS and IHS for all, image and

Cleaup and

Figure 1. Flow chart of the algorithm for the analysis of TSI images.

Formatted: Justified

Figure 2⁄1 Two examples for image preparation. The left column develops an image from SGP 17 April 2018 17:45:00 UTC, the right image was taken on SGP 3 April 2018 19:09:30 UTC. Top row: original image; centre row: image after colour correction, distortion removal, masking of horizon and equipment, and sun mark were applied; bottom row: final local sky map with sun at centre and a width of about 80 LSM units.

82
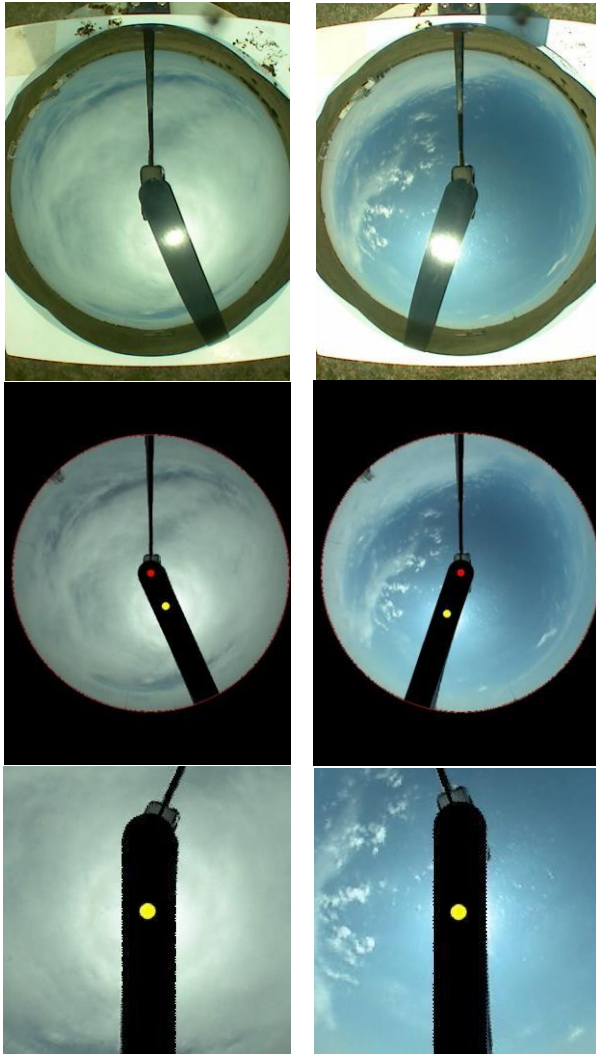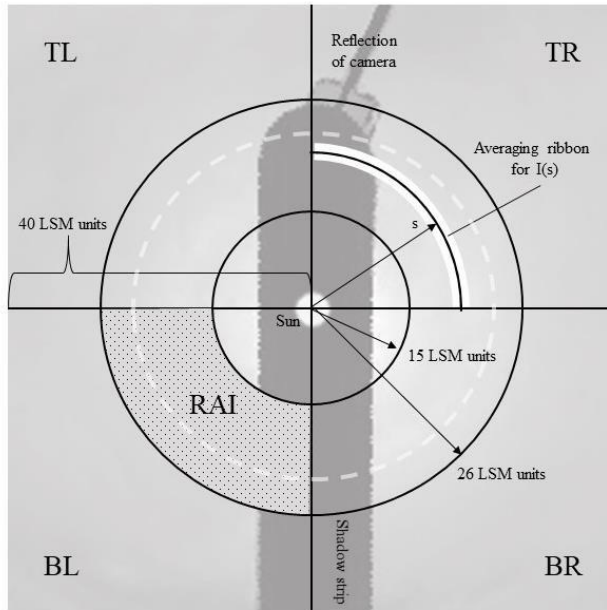
Figure 32. Layout of the local sky map (LSM). The LSM is divided into four quadrants, named according to their position as TR _ top right, BR _ bottom right, BL _ bottom left, and TL _ top left. The RAI is the Radial Analysis Interval for which STS and IHS properties are evaluated. The approximate position of the halo maximum is sketched in light gray. Shadow strip and camera are excluded from analysis.

5
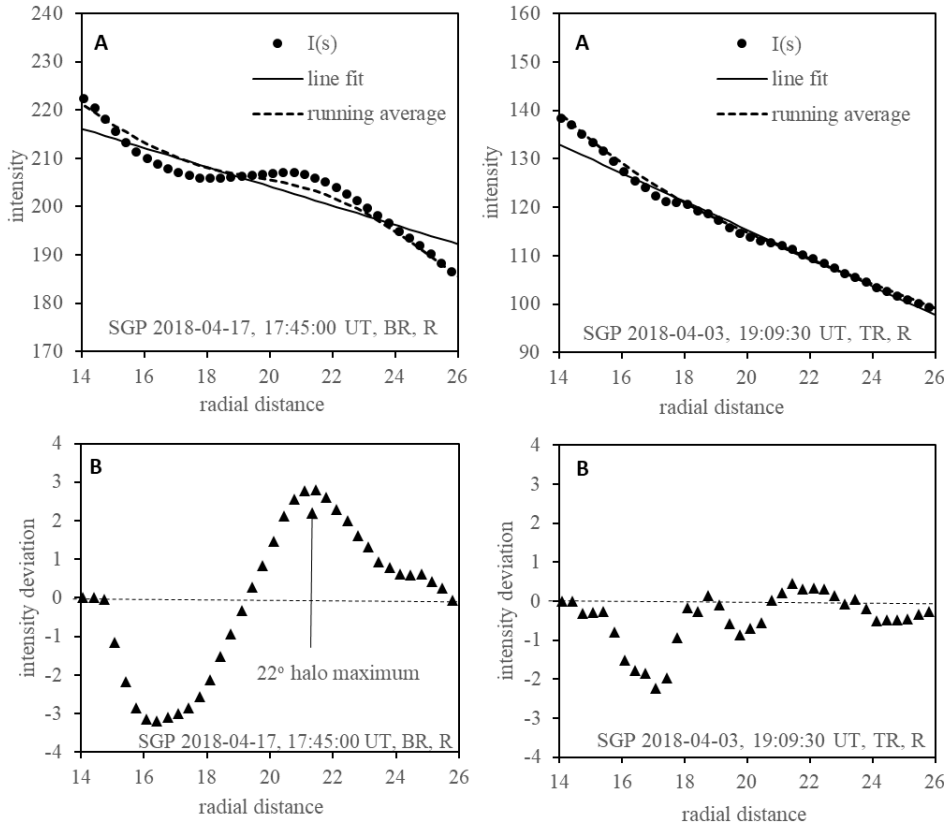
Figure 4̶3̶ Average radial intensity of the red channel is shown versus radial distance s , measured in LSM units, for the two images of Figure 1̶Fig. 2, halo at left. Panel (A) includes the average intensity $I(s)$, a linear fit, and the running average $I_6(s)$ as averaged over a width of 6 LSM units. (B) shows the radial intensity deviation $\eta(s)$. The halo signal is visible as a minimum at 17 LSM units, followed by a maximum at 21 LSM units in the left column.
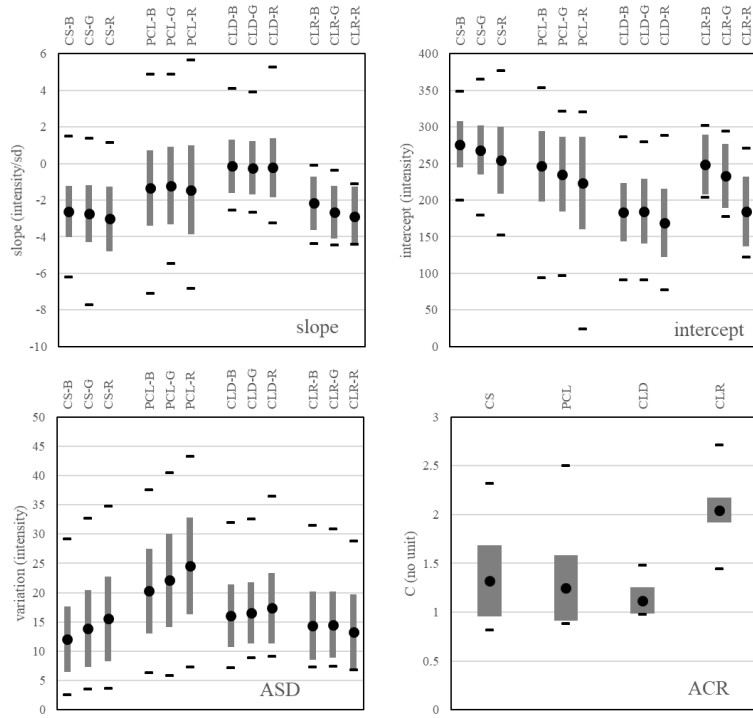
5

Figure 54 Sky type properties for the four sky types in the master table. Slope and intercept (top row) for the radial fit; areal standard deviation (ASD) of brightness (bottom left); average colour ratio (ACR) (bottom right). Sky types were assigned visually.

5 **Black circles indicate the mean, grey boxes the range of the first standard deviation, black bars limit the extreme values found in the master table.**
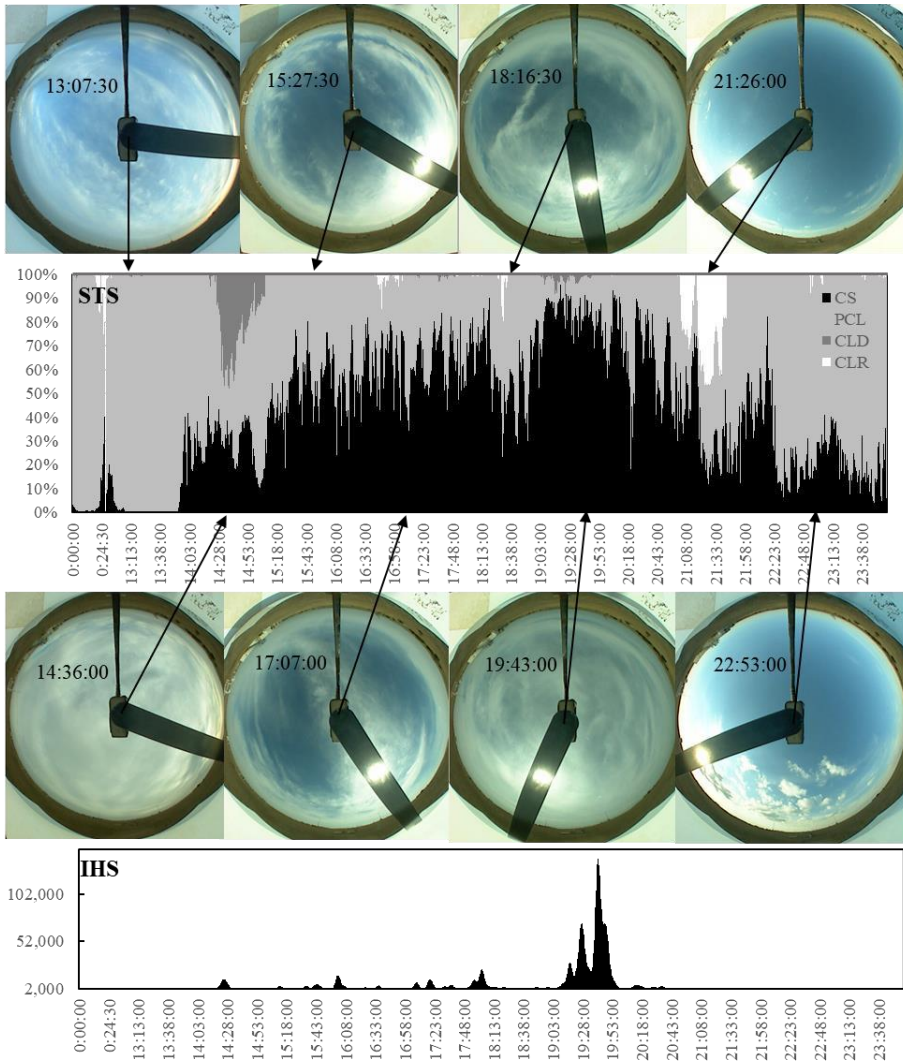
Figure 65 One-day example for STS and IHS (SGP March 10, 2018). Sample TSI images are included. The middle panel shows STS versus time of day (N/A excluded). Bottom panel shows the IHS versus time. All times in UTC.
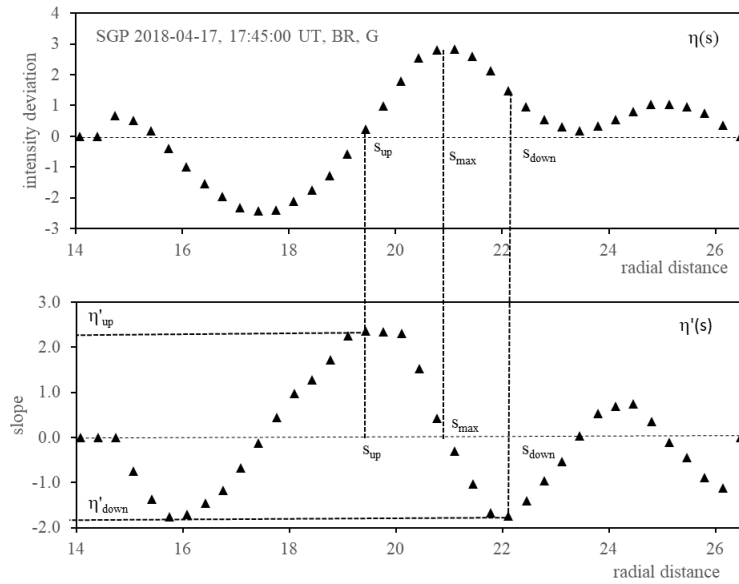
Figure 76. Radial markers used in halo scoring. The data belong to the green channel of the TSI image from SGP, April 17, 2018, see ~~Figure 1~~Fig. 2. The top panel shows the radial intensity deviation $\eta(s)$; the bottom panel shows its derivative $\eta'(s)$. Units are colour value units (0 to 255) for the intensity, and LSM units for the radial distance. The sequence of radial locations used in halo scoring is indicated, as well as the interpretation of the up- and down-slope markers.
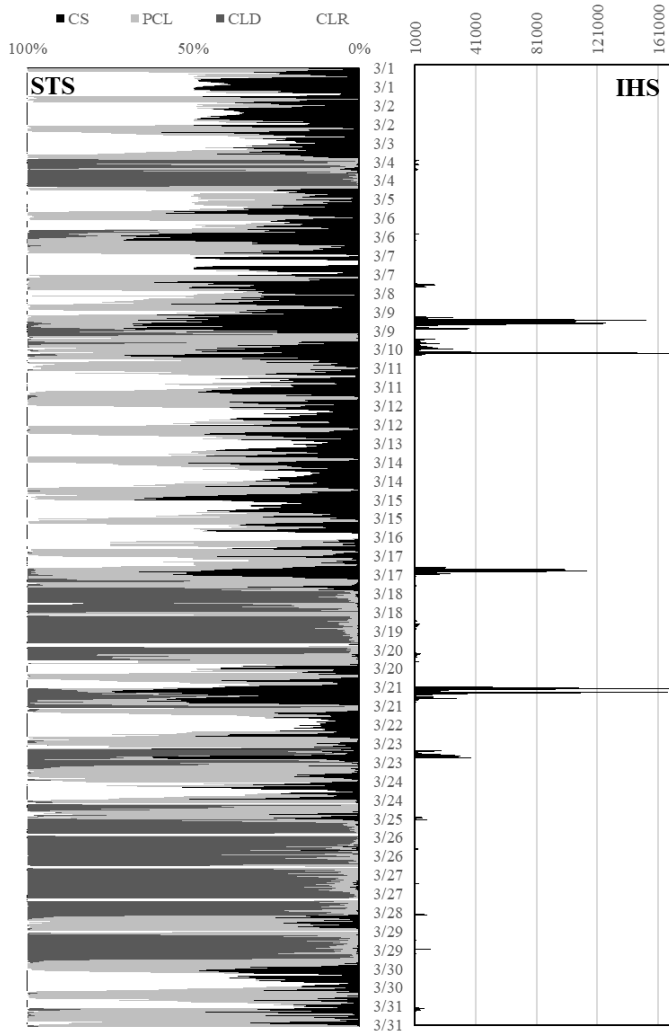
Figure 87. Time line of Sky type scores (STS) and ice halo scores (IHS) for TSI images from SGP March 2018 . Left panel shows the

STS: CS – black, PCL – light grey, CLD – dark grey, CLR – white. Right panel: IHS Pre-factor $C=10^6$, broadening w=3.5 minutes.
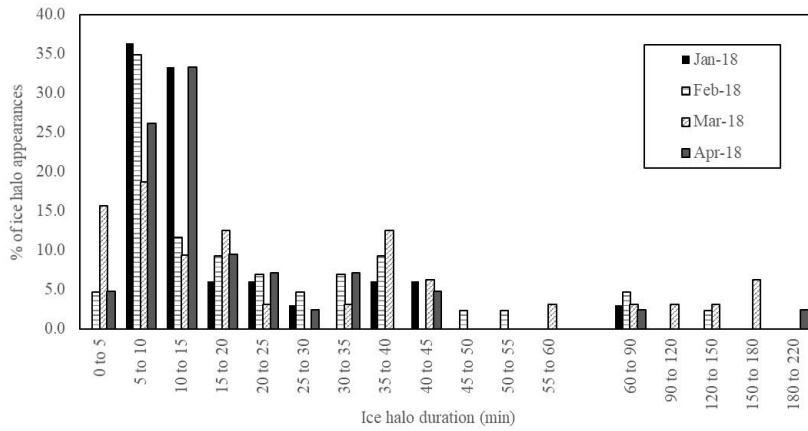
Figure 98. Distribution of observed 22°halo durations for the first four months of 2018 at SGP ARM site.

Marked up version of manuscript